OGLE-2018-BLG-0799Lb: a $q \sim 2.7 \times 10^{-3}$ planet with *Spitzer* parallax

Weicheng Zang,[1]⋆†‡§ Yossi Shvartzvald,[2]†§|| Andrzej Udalski,[3]¶ Jennifer C. Yee,[4]†§||
Chung-Uk Lee,[5,6]§ Takahiro Sumi,[7]|| Xiangyu Zhang,[1] Hongjing Yang,[1] Shude Mao,[1,8]||
Sebastiano Calchi Novati,[9]† Andrew Gould,[10,11]†§ Wei Zhu,[12]† Charles A. Beichman,[9]†
Geoffery Bryden,[13]† Sean Carey,[9]† B. Scott Gaudi,[11]† Calen B. Henderson,[9]† Przemek Mróz,[14]‡
Jan Skowron,[3]‡ Radoslaw Poleski,[3]‡ Michał K. Szymański,[3]‡ Igor Soszyński,[3]‡
Paweł Pietrukowicz,[3]‡ Szymon Kozłowski,[3]‡ Krzysztof Ulaczyk,[15]‡ Krzysztof A. Rybicki,[3]‡
Patryk Iwanek,[3]‡ Marcin Wrona,[3]‡ Michael D. Albrow,[16]§ Sun-Ju Chung,[5,6]§ Cheongho Han,[17]§
Kyu-Ha Hwang,[5]§ Youn Kil Jung,[5]§ Yoon-Hyun Ryu,[5]§ In-Gu Shin,[5]§ Sang-Mok Cha,[5,18]§
Dong-Jin Kim,[5]§ Hyoun-Woo Kim,[5]§ Seung-Lee Kim,[5,6]§ Dong-Joo Lee,[5]§ Yongseok Lee,[5,18]§
Byeong-Gon Park,[5,6]§ Richard W. Pogge,[11]§ Ian A. Bond,[19]¶ Fumio Abe,[20]¶ Richard Barry,[21]¶ David
P. Bennett,[21,22]¶ Aparna Bhattacharya,[21,22]¶ Martin Donachie,[23]¶ Hirosane Fujii,[7]¶ Akihiko Fukui,[24,25]¶
Yuki Hirao,[7]¶ Yoshitaka Itow,[20]¶ Rintaro Kirikawa,[7]¶ Iona Kondo,[7]¶ Naoki Koshimoto,[26,27]¶ Man
Cheung Alex Li,[23]¶ Yutaka Matsubara,[20]¶ Yasushi Muraki,[20]¶ Shota Miyazaki,[7]¶ Clément Ranc,[21]¶
Nicholas J. Rattenbury,[23]¶ Yuki Satoh,[7]¶ Hikaru Shoji,[7]¶ Daisuke Suzuki,[29]¶ Yuzuru Tanaka,[7]¶ Paul
J. Tristram,[30]¶ Tsubasa Yamawaki,[7]¶ Atsunori Yonehara,[31]¶ Etienne Bachelet,[32]|| Markus
P.G. Hundertmark,[33]|| R. Figuera Jaimes,[34,1]|| Dan Maoz,[35]|| Matthew T. Penny,[36]|| Rachel A. Street[32]||
and Yiannis Tsapras[33]||

Affiliations are listed at the end of the paper

ABSTRACT

We report the discovery and analysis of a planet in the microlensing event OGLE-2018-BLG-0799. The planetary signal was observed by several ground-based telescopes, and the planet-host mass ratio is $q = (2.65 \pm 0.16) \times 10^{-3}$. The ground-based observations yield a constraint on the angular Einstein radius θ_E, and the microlensing parallax vector π_E, is strongly constrained by the *Spitzer* data. However, the 2019 *Spitzer* baseline data reveal systematics in the *Spitzer* photometry, so there is ambiguity in the magnitude of the parallax. In our preferred interpretation, a full Bayesian analysis using a Galactic model indicates that the planetary system is composed of an $M_{planet} = 0.26^{+0.22}_{-0.11} M_J$ planet orbiting an $M_{host} = 0.093^{+0.082}_{-0.038}$ M$_\odot$, at a distance of $D_L = 3.71^{+3.24}_{-1.70}$ kpc. An alternate interpretation of the data shifts the localization of the minima along the arc-shaped microlens parallax constraints. This, in turn, yields a more massive host with median mass of 0.13 M$_\odot$ at a distance of 6.3 kpc. This analysis demonstrates the robustness of the osculating circles formalism, but shows that further investigation is needed to assess how systematics affect the specific localization of the microlens parallax vector and, consequently, the inferred physical parameters.

Key words: gravitational lensing: micro – planets and satellites: detection.

1 INTRODUCTION

Very low mass (VLM; $M \leq 0.2$ M$_\odot$) dwarfs represent the lower mass end of star formation through the process of collapsing molecular clouds (e.g. Luhman 2012), so studying planets around VLM dwarfs can test different planet formation theories in limiting conditions (e.g. Ida & Lin 2005; Boss 2006). Due to the intrinsic faintness of VLM dwarfs, the detection of planets around them is challenging for most of exoplanet detection methods such as the transit and the radial velocity methods. Although microlening planets comprise a minor fraction (~ 2.2 per cent[1]) of all known planets, the technique plays an important role in probing planets orbiting VLM dwarfs because it does not rely on the light from the host stars but rather uses the

⋆ E-mail: 3130102785@zju.edu.cn
† The *Spitzer* Team.
‡ The KMTNet Collaboration.
§ The LCO/*Spitzer* Follow-up Team.
¶ The OGLE Collaboration.
|| The MOA Collaboration.

[1] http://exoplanetarchive.ipac.caltech.edu as of 2020 October 10.

light from a background source (Mao & Paczynski 1991; Gould & Loeb 1992). Among the 81 confirmed planets orbiting a VLM dwarf, 29 of them were found by the microlensing method. However, only seven such microlens planetary systems have unambiguous mass measurements: MOA-2007-BLG-192 (Bennett et al. 2008; Kubas et al. 2012), MOA-2010-BLG-073 (Street et al. 2013), OGLE-2012-BLG-0358 (Han et al. 2013), OGLE-2013-BLG-0102 (Jung et al. 2015), OGLE-2013-BLG-0341 (Jung et al. 2015), MOA-2013-BLG-605 (Sumi et al. 2016), OGLE-2016-BLG-1195 (Bond et al. 2017; Shvartzvald et al. 2017), while other systems require a Bayesian analysis based on a Galactic model to estimate the mass of the planetary systems.

The mass measurement of a microlens lens system is challenging. To measure the mass of a lens system, one needs two observables that yield mass–distance relations for the lens systems, i.e. any two of the angular Einstein radius θ_E, the microlens parallax π_E and the apparent brightness of the lens system. The detection of lens brightness can be achieved by high angular resolution imaging when the source and lens are resolved (e.g. Alcock et al. 2001; Kozłowski et al. 2007; Batista et al. 2015; Bennett et al. 2015; Bhattacharya et al. 2018; Bennett et al. 2020; Bhattacharya et al. 2020; Vandorou et al. 2020; Terry et al. 2021), but it is difficult for very faint VLM dwarfs. The measurements of θ_E and π_E can yield the mass of a lensing object by (Gould 2000)

$$M_L = \frac{\theta_E}{\kappa \pi_E}, \tag{1}$$

and its distance by

$$D_L = \frac{\mathrm{AU}}{\pi_{rel} + \pi_S}, \qquad \pi_{rel} = \pi_E \theta_E, \tag{2}$$

where $\kappa \equiv 4G/(c^2 \mathrm{AU}) = 8.144$ mas $M_\odot^{-1}$, $\pi_S = \mathrm{AU}/D_S$ is the source parallax, D_S is the source distance (Gould 1992, 2004), and π_{rel} is the lens–source relative parallax. The measurements of angular Einstein radii θ_E are mainly via finite-source effects when the source crosses or approaches a caustic along the line of sight (Gould 1994; Nemiroff & Wickramasinghe 1994; Witt & Mao 1994), which are frequently detected in binary/planetary events because of their relatively large caustic structures. For the 29 microlens planet-VLM events, 24 of them have measurements of finite-source effects and thus the angular Einstein radius θ_E. The microlens parallax π_E can be measured by the annual parallax effect (Gould 1992), in which Earth's acceleration around the Sun introduces deviation from rectilinear motion to the lens–source relative motion. This method is generally feasible for events with long microlensing time-scales $t_E \gtrsim \mathrm{year}/2\pi$ (e.g. Gaudi et al. 2008; Bennett et al. 2010) and/or events produced by nearby lenses (e.g. Jung et al. 2018). However, because the typical microlensing time-scales for VLM events are $\lesssim 20$ d (see equation 17 of Mao 2012), measurements of the annual parallax for planet-VLM events are challenging and only six of such events have a robust detection of annual parallax.

Microlens parallax π_E can also be measured via 'satellite microlens parallax', which is done by observing the same microlensing event from Earth and one or more well-separated ($\sim$ AU) satellite (Refsdal 1966; Gould 1994, 1995). The feasibility of satellite microlens parallax measurements has been demonstrated by the *Spitzer* satellite telescope (Dong et al. 2007; Calchi Novati et al. 2015a; Yee et al. 2015a; Udalski et al. 2015b; Zhu et al. 2015), the two-wheel *Kepler* satellite telescope (Zhu et al. 2017a; Zang et al. 2018; Poleski et al. 2019), the *Gaia* satellite (Wyrzykowski et al. 2020) and the joint observations of *Spitzer* and *Kepler* (Zhu et al. 2017c). Since 2014, the *Spitzer* satellite observed about 1100

microlensing events and yielded satellite parallax measurements for ten microlens planetary events: OGLE-2014-BLG-0124 (Udalski et al. 2015b; Beaulieu et al. 2018), OGLE-2015-BLG-0966 (Street et al. 2016), OGLE-2016-BLG-1067 (Calchi Novati et al. 2019), OGLE-2016-BLG-1190 (Ryu et al. 2018), OGLE-2016-BLG-1195 (Bond et al. 2017; Shvartzvald et al. 2017), OGLE-2017-BLG-0406 (Hirao et al. 2020), OGLE-2017-BLG-1140 (Calchi Novati et al. 2018), OGLE-2018-BLG-0596 (Jung et al. 2019), KMT-2018-BLG-0029 (Gould et al. 2020), and Kojima-1 (Nucita et al. 2018; Fukui et al. 2019; Zang et al. 2020b). In particular, for OGLE-2016-BLG-1195, the *Spitzer* satellite parallax combined with the measurements of θ_E from ground-based data revealed that this planetary system is composed of an Earth-mass ($\sim 1.4\,M_\oplus$) planet around an $\sim 0.078\,M_\odot$ ultracool dwarf with a lens distance of ~ 3.9 kpc.

Here we report the analysis of the second *Spitzer* planet orbiting a VLM dwarf, OGLE-2018-BLG-0799Lb. This paper is structured as follows. In Section 2, we describe the ground-based and *Spitzer* observations of the event. We then fit the ground-based data in Section 3 and fit the *Spitzer* satellite parallax in Section 4. We estimate the physical parameters of the planetary system in Section 5. Finally, implications of this work and discussion are given in Sections 6 and 7, respectively.

2 OBSERVATIONS AND DATA REDUCTIONS

2.1 Ground-based observations

OGLE-2018-BLG-0799 was first discovered by the Optical Gravitational Lensing Experiment (OGLE) collaboration (Udalski, Szymański & Szymański 2015a) and alerted by the OGLE Early Warning System (Udalski et al. 1994; Udalski 2003) on 2018 May 13. The event was located at equatorial coordinates $(\alpha, \delta)_{\mathrm{J2000}} = (18:13:50.16, -25:29:08.6)$, corresponding to Galactic coordinates $(\ell, b) = (6.12, -3.73)$. It therefore lies in OGLE field BLG545, with a cadence of 0.5–1 observations per night. These data were taken using the 1.3-m Warsaw Telescope equipped with a 1.4 deg^2 FOV mosaic CCD camera at the Las Campanas Observatory in Chile (Udalski et al. 2015a). About 50 d after OGLE's alert, the Microlensing Observations in Astrophysics (MOA; Bond et al. 2001) group also identified this event as MOA-2018-BLG-215. The MOA group conducts a high-cadence survey toward the Galactic bulge using its 1.8-m telescope equipped with a 2.2 deg^2 FOV camera at the Mt. John University Observatory in New Zealand (Sumi et al. 2016). The cadence of the MOA group for this event is $\Gamma \sim 1$ h^{-1} on average. This event was also observed by the Korea Microlensing Telescope Network (KMTNet) that consists of three 1.6-m telescopes equipped with 4 deg^2 FOV cameras at the Cerro Tololo Inter-American Observatory (CTIO) in Chile (KMTC), the South African Astronomical Observatory (SAAO) in South Africa (KMTS) and the Siding Spring Observatory (SSO) in Australia (KMTA; Kim et al. 2016). It was recognized after the end of the 2018 season by KMTNet's event-finding algorithm as KMT-2018-BLG-1741 (Kim et al. 2018). The event lies in the KMTNet BLG31 field, which has a nominal cadence of $\Gamma = 0.4$ h^{-1}. However, from the start of the season through 2018 June 25, the cadence of KMTA and KMTS was altered to $\Gamma = 0.3$ h^{-1}. Thus, the second half of the light curve (including the planetary anomaly) has a higher cadence than the first half. The great majority of data were taken in the I band for OGLE and KMTNet groups, and MOA-Red filter (which is similar to the sum of the standard Cousins R- and I-band filters) for the MOA group, with occasional observations made in the V band for measurement of the source colour.

Table 1. Data used in our analysis.

Collaboration	Site	Filter	Coverage (HJD$'$)	N_{data}	Reduction method
OGLE		I	7800–8398	158	Wozniak ([2000](#))
MOA		Red	8157–8392	486	Bond et al. ([2001](#))
KMTNet	SSO	I	8171–8400	295	pySIS (Albrow et al. [2009](#))
	CTIO	I	8169–8412	435	pySIS (Albrow et al. [2009](#))
	CTIO	I	8169–8412	435	pyDIA
	CTIO	V	8176–8409	44	pyDIA
	SAAO	I	8172–8402	259	pySIS (Albrow et al. [2009](#))
CT13		I	8287–8329	49	DOPHOT (Schechter, Mateo & Saha [1993](#))
LCO	SSO	i	8302–8310	26	DanDIA (Bramich [2008](#))
	CTIO	i	8300–8311	20	DanDIA (Bramich [2008](#))
Spitzer		L	8308–8690	36	Calchi Novati et al. ([2015b](#))

Note. HJD$'$ = HJD − 2450000

On 2018 June 30 (UT 23:18), the *Spitzer* team realized that OGLE-2018-BLG-0799 was deviating from the point-lens point-source model based on the KMTNet observations taken in the previous 24 h. At that point, they scheduled high-cadence follow-up observations by Las Cumbres Observatory (LCO) global network of telescopes and the 1.3-m SMARTS telescope equipped with the optical/NIR ANDICAM camera at CTIO (CT13; DePoy et al. [2003](#)). For this event, the LCO observations were taken by the 1-m telescopes in CTIO and SSO, and the 0.4-m telescopes in SSO, with SDSS-i' filter. The majority of CT13 observations were taken in the I and H bands, with occasional observations in the V band. The LCO 0.4-m, CT13 V- and H-band data were excluded from the analysis due to excessive noise. In Table [1](#), we list details about the data used in the analysis.

2.2 *Spitzer* observations

The goal of the *Spitzer* microlensing parallax program is to create an unbiased sample of microlensing events with well-measured parallax. In order to isolate the knowledge of the presence or absence of planets from influencing event selections, Yee et al. ([2015b](#)) developed protocols for selecting *Spitzer* targets. There are three ways an event may be selected for *Spitzer* observations. First, events that meet the specified objective criteria are selected as 'objective' targets and *must* be observed with a pre-specified cadence. Second, events that do not meet these criteria can still be chosen as 'subjective' targets *at any time for any reason*, but only data taken (or rather, made public) after this selection date can be used to calculate the planetary sensitivity of the events. The *Spitzer* team can publicly announce specified conditions for a candidate 'subjective' target, and targets that obey the conditions are then automatically selected as a 'subjective' target. 'Subjective' selection is crucial because the 'objective' criteria must be strictly defined so that all the 'objective' targets have both high sensitivity to planets and a high likelihood of yielding a parallax measurement. In some cases, an event may never become objective but still be a good candidate. In addition, *Spitzer* observations that start a week or two earlier may improve the parallax measurement for an event that will meet the 'objective' criteria later. Finally, events can be selected as 'secret' targets without any announcement and become 'subjectively selected' after the *Spitzer* team makes a public announcement.

Although OGLE-2018-BLG-0799 was recognized as a promising target early on, observations could not begin until July 9 due to Sun-angle constraints (the target is in the far western side of the bulge). It was announced as a candidate 'subjective' *Spitzer* target on 2018 June 12, with a specified condition: If the I-band magnitude is brighter than 16.85 mag at HJD$'$ = 8301.5 (HJD$'$ = HJD − 2450000), the

event would be 'subjectively' selected. The event met this condition with I = 16.36 at HJD$'$ = 8301.5. However, it did not meet the objective criteria because it had already peaked at $A_{max} < 3$. Each *Spitzer* observation was composed of six dithered 30-s exposures using the 3.6-μm channel (L band) of the IRAC camera. *Spitzer* observed this event 31 times with a daily cadence in 2018. In order to test for systematic errors pointed out by Zhu et al. ([2017b](#)) and Koshimoto & Bennett ([2020](#)) (see Section [4.1](#) for details), OGLE-2018-BLG-0799 was reobserved at baseline five times over 8 d near the beginning of the 2019 observing window.

2.3 Data reduction

Data reductions of the OGLE, MOA, KMTNet, and LCO data sets were conducted using custom implementations of the difference image analysis technique (Tomaney & Crotts [1996](#); Alard & Lupton [1998](#)): Wozniak [2000](#) (OGLE), Bond et al. [2001](#) (MOA), Albrow et al. [2009](#) (KMTNet), and Bramich [2008](#) (LCO). The CT13 data were reduced using DOPHOT (Schechter et al. [1993](#)). The *Spitzer* data were reduced using specially designed software for crowded-field photometry (Calchi Novati et al. [2015b](#)). In addition, to measure the source colour and construct the colour–magnitude diagram (CMD), we conduct pyDIA photometry[2] for the KMTC data, which yields field-star photometry on the same system as the light curve.

3 GROUND-BASED LIGHT-CURVE ANALYSIS

Fig. [1](#) shows the observed data together with the best-fitting models. The ground-based light curve shows a bump (HJD$'$ ∼8300) after the peak of an otherwise normal point-lens point-source light curve. The bump could be a binary-lensing (2L1S) anomaly or the second peak of a binary-source event (1L2S). Thus, we perform both 2L1S and 1L2S analysis in this section. Finally, in order to compare parallax constraints from ground-based data and *Spitzer* data to check against possible systematics in either data set, we fit the annual parallax effect in Section [3.3](#).

3.1 Static binary-lens model

A 'static' binary-lens model requires seven geometric parameters to calculate the magnification, $A(t)$. These include three point-lens

---

[2]MichaelDAlbrow/pyDIA: Initial Release on Github, doi:10.5281/zenodo.268049.
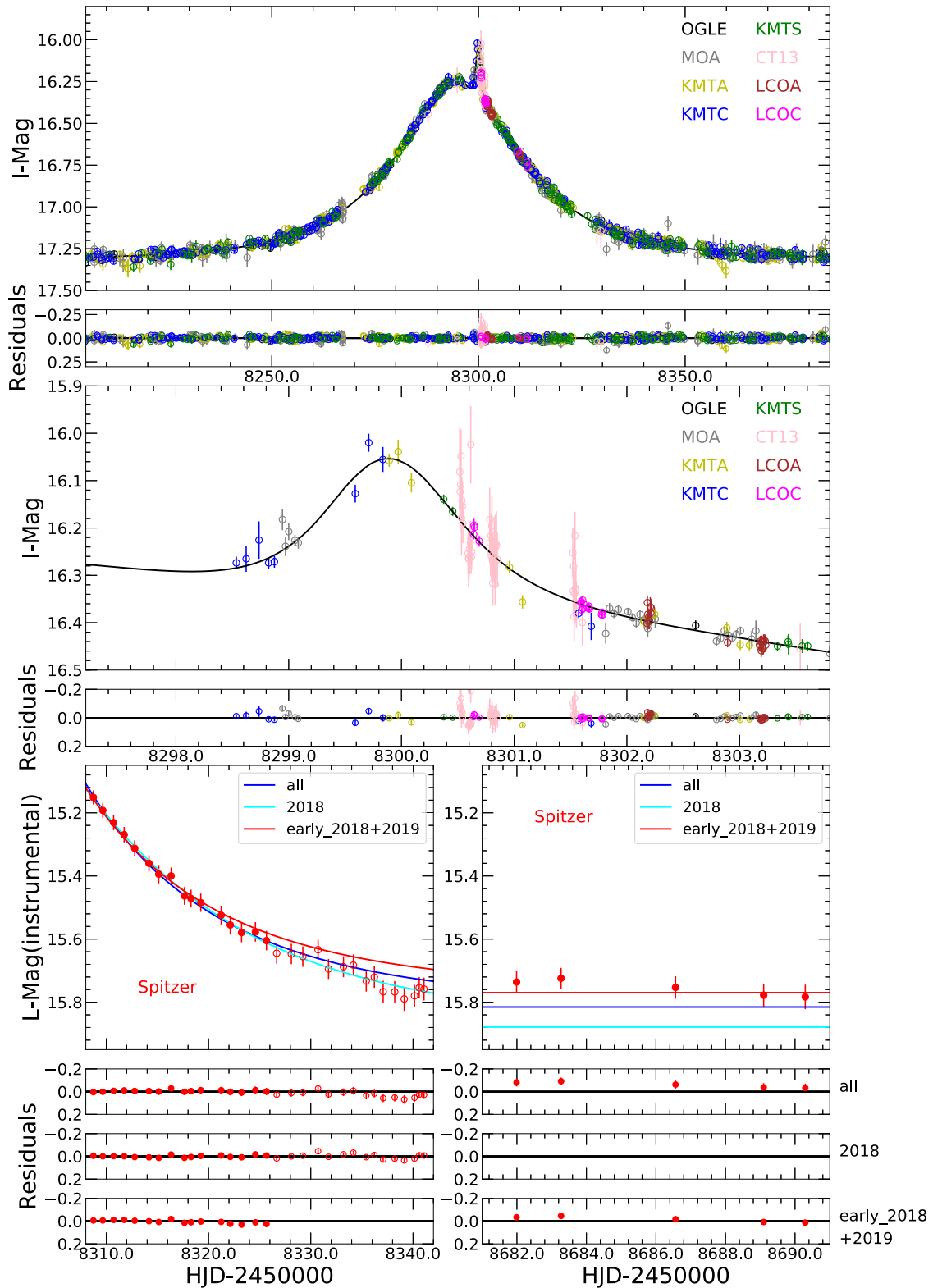
Figure 1. The observed data with the best-fitting 2L1S model. The circles with different colours are observed data points for different data sets. The black solid line represents the best-fitting model for the ground-based data. The middle panel shows a close-up of the planetary signal. The bottom panels show *Spitzer* observations with the residuals from the best-fitting models. The *Spitzer* data in the 'early_2018 + 2019' subset are shown as filled, red circles, while the 'late 2018' data are shown as open circles. The best-fitting models for each subset of the data '2018-only', 'early_2018 + 2019', and 'all' are shown as the cyan, red, and blue lines, respectively.
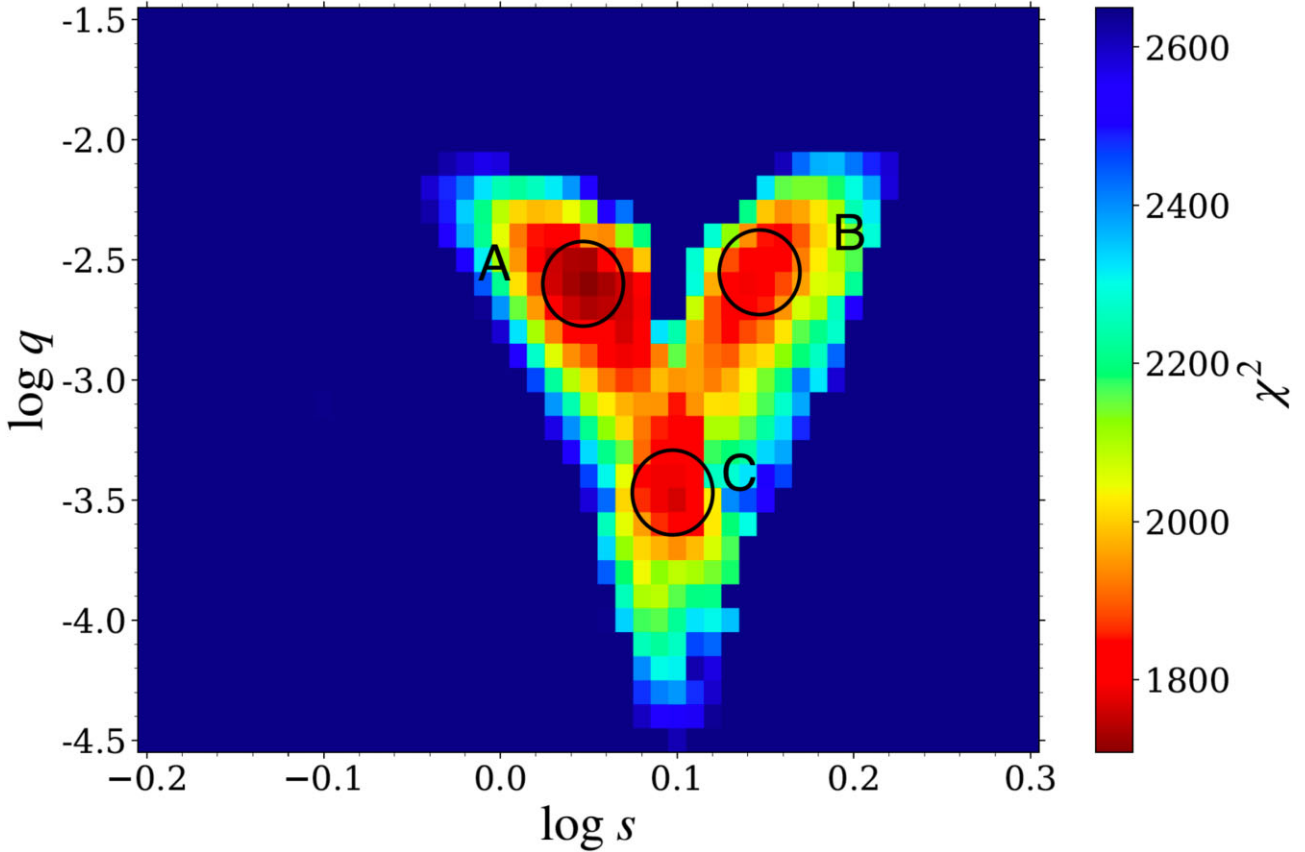
Figure 2. χ^2 surface in the (log s, log q) plane from the grid search. The space is equally divided on a (51 × 31) grid with ranges of $-0.2 \leq \log s \leq 0.3$ and $-4.5 \leq \log q \leq -1.5$, respectively. The black circles labelled as A, B, and C in the right-hand panel represent three distinct minima.

parameters (Paczyński 1986)): the time of the maximum magnification, t_0, the minimum impact parameter, u_0, which is in units of the angular Einstein radius θ_E, and the Einstein radius crossing time, t_E. There are four additional parameters: the angular radius of the source star, ρ, in units of θ_E; mass ratio of the binary, q; the projected separation, s, between the binary components normalized to θ_E; and the angle of source trajectory relative to the binary axis in the lens plane, α. We use the advanced contour integration code (Bozza 2010; Bozza et al. 2018), VBBinaryLensing³ to compute the binary-lens magnification $A(t)$. In addition, for each data set i, there are two linear parameters $(f_{S,i}, f_{B,i})$ representing the flux of the source star and any blended flux, respectively. Hence, the observed flux $f_i(t)$ is modelled as

$$f_i(t) = f_{S,i}A(t) + f_{B,i}. \qquad (3)$$

In addition, we adopt a linear limb-darkening law to consider the brightness profile of the source star (An et al. 2002). According to the extinction-corrected source colour and the colour–temperature relation of Houdashelt, Bell & Sweigart (2000), we estimate the effective temperature of the source to be $T_{eff} \sim 4900$ K. Applying ATLAS models (Claret & Bloemen 2011), we obtain the linear limb-darkening coefficients $u_I = 0.56$ for the I band, $u_{i'} = 0.58$ for the SDSS-i' band, $u_R = 0.66$ for the R band (Claret & Bloemen 2011). For the MOA data, we adopt $\Gamma_{MOA} = (\Gamma_I + \Gamma_R)/2 = 0.61$.

To search the parameter space of 2L1S models, we first carry out a sparse grid search on parameters (log s, log q, α, log ρ), with 21

³http://www.fisica.unisa.it/GravitationAstrophysics/VBBinaryLensing.htm.

values equally spaced within $-1 \leq \log s \leq 1$, $0° \leq \alpha < 360°$, 51 values equally spaced within $-5 \leq \log q \leq 0$ and 8 values equally spaced within $-3 \leq \log \rho \leq -1$, respectively. For each set of (log s, log q, α, log ρ), we fix log q, log s, log ρ, with t_0, u_0, t_E, α free. We find the minimum χ^2 by Markov chain Monte Carlo (MCMC) χ^2 minimization using the EMCEE ensemble sampler (Foreman-Mackey et al. 2013). The sparse grid search shows that the distinct minima are within $-0.2 \leq \log s \leq 0.3$ and $-4.5 \leq \log q \leq -1.5$. We then conduct a denser grid search, which consists of 51 values equally spaced within $-0.2 \leq \log s \leq 0.3$, and 31 values equally spaced within $-4.5 \leq \log q \leq -1.5$. As a result, we find three distinct minima and label them as models A, B, and C in Fig. 2.

We then investigate the best-fitting models by MCMC with all geometric parameters free. Finally, model A (log s, log q) = (0.048 ± 0.003, −2.58 ± 0.02) provides the best fit to the observed data, while model B (log s, log q) = (0.151 ± 0.002, −2.53 ± 0.02) and model C (log s, log q) = (0.093 ± 0.002, −3.46 ± 0.02) are disfavored by $\Delta\chi^2 \sim 68$ and ~61, respectively. In addition, finite-source effects of model A are marginally detected. The modelling only provides an upper limit on the source size normalized by the Einstein radius, $\rho < 0.026$ (3σ level). The best-fitting model has $\rho = 0.016$, but the data are also marginally consistent with a point-source model at $\Delta\chi^2 = 7$. Likewise for model B, the best-fitting value of ρ is 0.0002 but is consistent with zero in 1σ and has a 3σ upper limit of 0.010. For model C, finite source effects are measured to be $\rho = 0.0303 ± 0.0009$. The best-fitting parameters of the three models are given in Table 2, and the caustic geometries of the three models are shown in Fig. 3.

Table 2. Best-fitting models and their 68 per cent uncertainty ranges from MCMC for ground-only data.

Models	2L1S			1L2S
	A	B	C	
χ^2/d.o.f.	1704.8/1705	1771.5/1705	1765.8/1705	1861.7/1704
$t_{0,1}$ (HJD$'$)	8295.15 ± 0.02	8295.26 ± 0.02	8295.10 ± 0.02	8294.87 ± 0.02
$t_{0,2}$ (HJD$'$)	...	...	...	8300.04 ± 0.04
$u_{0,1}$	0.403 ± 0.008	0.409 ± 0.009	0.397 ± 0.008	0.620 ± 0.041
$u_{0,2}$	...	...	...	0.000 ± 0.002
t_E (d)	28.2 ± 0.4	27.8 ± 0.4	28.7 ± 0.4	24.6 ± 1.0
s	1.116 ± 0.008	1.415 ± 0.007	1.239 ± 0.006	...
$q(10^{-3})$	2.62 ± 0.14	2.98 ± 0.15	0.345 ± 0.015	...
α (rad)	1.170 ± 0.003	1.178 ± 0.003	1.174 ± 0.003	...
ρ_1	<0.026	<0.010	0.0303 ± 0.0009	0.606 ± 0.050
ρ_2	...	...	...	0.020 ± 0.002
$q_{f,I}$	...	...	...	0.0049 ± 0.0003
$f_{S,OGLE}$	1.794 ± 0.047	1.850 ± 0.054	1.727 ± 0.049	2.372 ± 0.176
$f_{B,OGLE}$	−0.032 ± 0.046	−0.086 ± 0.052	0.034 ± 0.048	−0.612 ± 0.175

Notes. The values of ρ_1 are their 3σ upper limits. All fluxes are on an 18th magnitude scale, e.g. $I_S = 18 - 2.5\log(f_S)$. Ellipses means that the parameter is not included in the model.
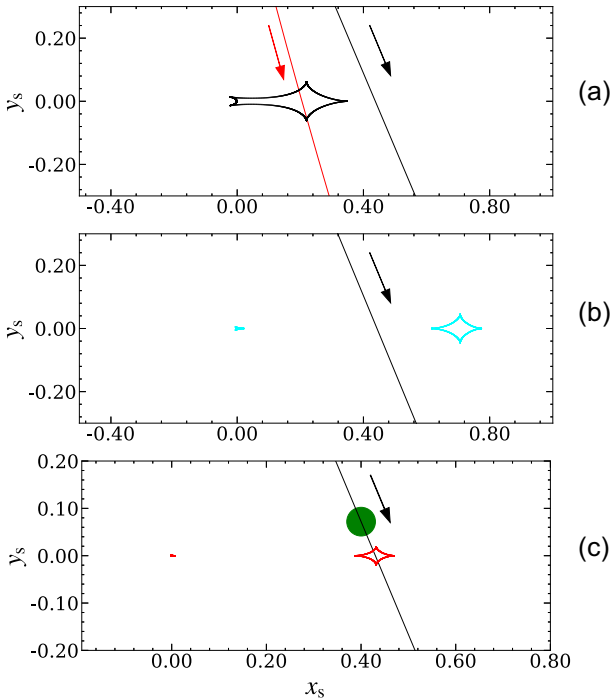
Figure 3. Caustic geometries of the three static 2L1S models. The caustics are colour-coded to match the light curves in the Fig. 5. The axes are in units of the Einstein radius θ_E. In each panel, the black solid line is the source trajectory seen from the ground, and the arrow indicates the direction of the source motion. In the top panel, the red solid line is the source trajectory seen from the *Spitzer* satellite. Because finite source effects are measured for model C, the radius of the green circle in the bottom panel represents the source radius $\rho = 0.0303$. Models A and B only have weak constraints on ρ (see Section 3.1), so their source radii are not shown.

We find that the MCMC does not jump from one model to the other in a normal run. To investigate the barriers between the three models and check for other potential degenerate models, we run a 'hotter' MCMC by artificially inflating the error bars by a factor of 5.0. The upper panel of Fig. 4 shows $\log q$ against the offset of the source trajectory from the planetary caustic centre (Hwang et al. 2018a, b;

Skowron et al. 2018):

$$\Delta\xi = u_0 \csc(\alpha) - \left(s - s^{-1}\right). \tag{4}$$

We find that the barriers between the three models have $\Delta\chi^2 > 125$ and there is no obvious additional model. We also note that the topology of Model C is characterized by a large source that crosses a planetary caustic. A similar topology and light curve were found in the planetary event OGLE-2017-BLG-0173, except that the corresponding Model C is split into two local minima (see fig. 4 of Hwang et al. 2018b). Thus, we further investigate model C using a 'hotter' MCMC with the error bars inflated by a factor of $\sqrt{5}$. The bottom panel of Fig. 4 shows the result, in which we do not find any further degeneracy.

While OGLE-2018-BLG-0799 is qualitatively similar to OGLE-2017-BLG-0173, there are also notable differences in the two cases. Both have a single planetary perturbation dominated by finite source effects rather than a distinct caustic entrance and exit. The resulting χ^2 surface in both cases has three minima, one in which the source passes directly over the planetary caustic (in the case of OGLE-2017-BLG-0173, this minimum is bimodal) and two in which the source passes to one side or the other of the planetary caustic. However, in the case of OGLE-2017-BLG-0173, in the solution with the source passing directly over the caustic, the source is much larger than the caustic, whereas in the solutions in which the source passes to one side or the other, the source size is comparable to the size of the caustic. By contrast, in the present case, when the source passes directly over the caustic, it is comparable in size to the caustic (see Fig. 3) but when it passes to one side of the other, it does not cross the caustic and there is only an upper limit on the source size. In addition, in OGLE-2017-BLG-0173, the degeneracies between the solutions cannot be definitely resolved, whereas in the present case, the degeneracy between the three solutions is clearly resolved by χ^2.

In Fig. 5, we show the residuals for the three models and draw the cumulative $\Delta\chi^2$ distribution of models B and C relative to model A over the anomaly region. We find that most of the χ^2 differences are from the short-lived bump, and models B and C cannot well fit the data over the anomaly region. We also check whether the $\Delta\chi^2$ can be decreased by considering the parallax effect, but all of models in Sections 3.3 and 4 have $\Delta\chi^2 > 60$ for models B and C. Thus, we exclude models B and C.
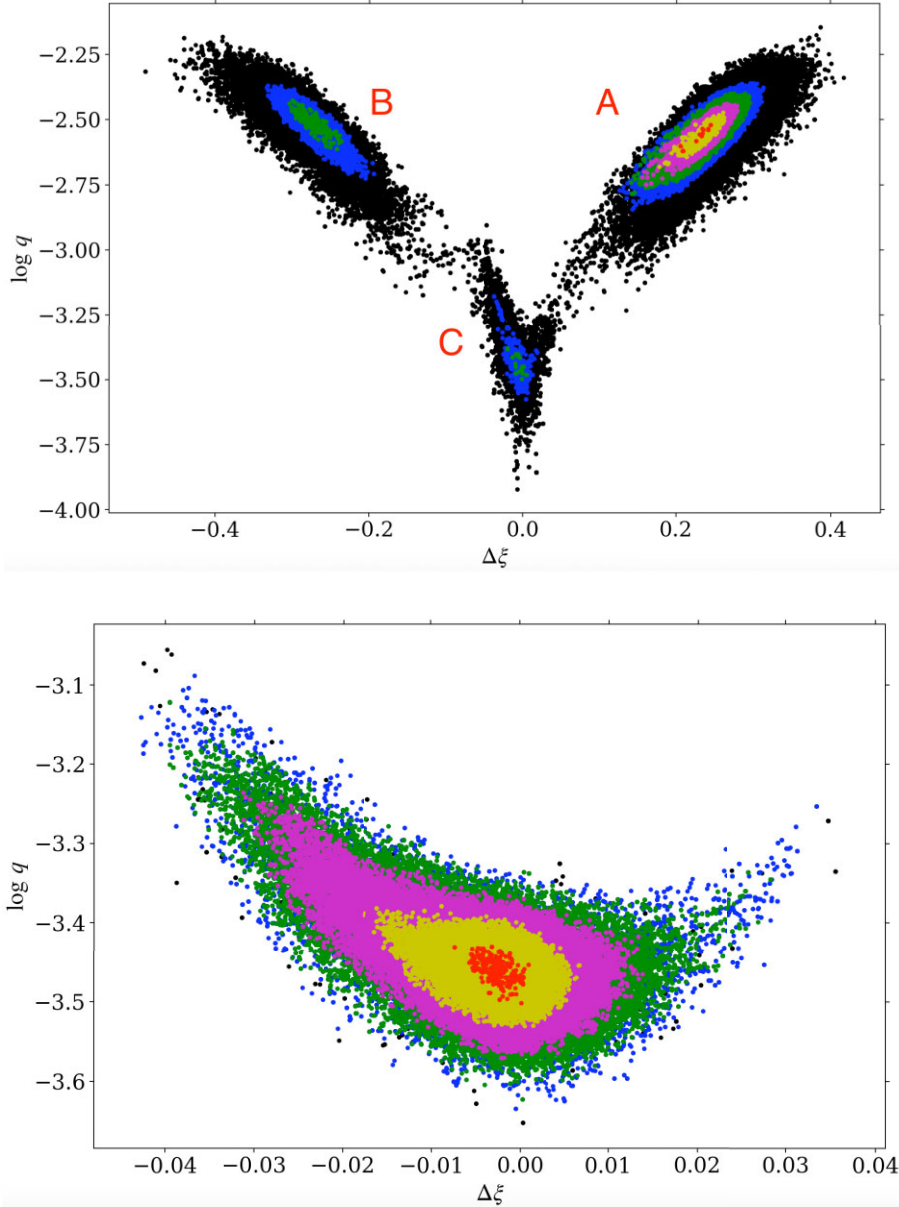
Figure 4. Scatter plot of $\Delta\xi$ versus $\log q$ from 'hotter' MCMC chains, where $\Delta\xi = u_0 \csc(\alpha) - (s - s^{-1})$ is the offset of the centre of the source from the centre of the caustic at the moment that the source crosses the binary axis. Upper panel: The result is derived by inflating the error bars by a factor of 5.0, and then multiplying the resulting χ^2 by 25 for the plot. Lower panel: The result is derived by inflating the error bars by a factor of $\sqrt{5}$, and then multiplying the resulting χ^2 by 5 for the plot. Note that the best-fitting solution shown in the upper panel is preferred over that shown in the lower panel by $\Delta\chi^2 = 61$. The purpose of the lower panel is to check whether the model C has a bimodal minimum similar to the corresponding model of OGLE-2017-BLG-0173 (Hwang et al. 2018b). In each panel, the initial parameters of the MCMC chain are the Model C shown in Table 2. Red, yellow, magenta, green, blue, and black colours represent $\Delta\chi^2 < 5 \times (1, 4, 9, 16, 25, \infty)$.

3.2 Binary-source model

Gaudi (1998) first pointed out that a binary-source event can also cause a smooth, short-lived, low-amplitude bump if the second source is much fainter and passes closer to the lens, which is similar to planet-induced anomalies. The total magnification of a 1L2S event is the superposition of two point-lens events:

$$A_\lambda = \frac{A_1 f_{1,\lambda} + A_2 f_{2,\lambda}}{f_{1,\lambda} + f_{2,\lambda}} = \frac{A_1 + q_{f,\lambda} A_2}{1 + q_{f,\lambda}}, \tag{5}$$

$$q_{f,\lambda} = \frac{f_{2,\lambda}}{f_{1,\lambda}}, \tag{6}$$

where $f_{i,\lambda}$ ($i = 1, 2$) is the flux at wavelength λ of each source and A_λ is total magnification (Hwang et al. 2013). The best-fitting 1L2S model is disfavored by $\Delta\chi^2 \sim 157$ compared to the 2L1S model A (see Table 2 for the parameters). In Fig. 5, we find that the χ^2 difference to the 2L1S model A is mainly from the short-lived bump and the 1L2S model fails to fit the observed data. Thus, we exclude the 1L2S model.
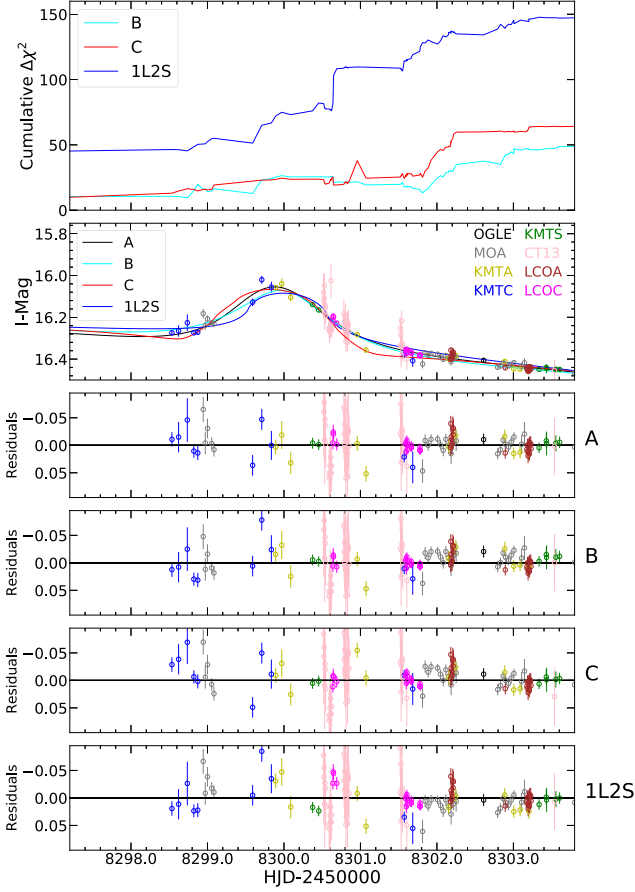
Figure 5. The upper panel shows the cumulative distribution of χ^2 differences for 2L1S and 1L2S models compared to the 2L1S Model A ($\Delta\chi^2 = \chi^2_{\text{model}} - \chi^2_A$) over the anomaly region. The second panel shows a close-up of the anomaly region, in which the lines with different colours represent the different models. The residuals for each model are shown separately in the bottom four panels.

3.3 Ground-based parallax

We fit the annual parallax effect by introducing two additional parameters $\pi_{E,N}$ and $\pi_{E,E}$, the north and east components of π_E in equatorial coordinates (Gould 2004). Because the annual parallax effect can be correlated with the effects of lens orbital motion, we also introduce two parameters (ds/dt, $d\alpha/dt$), the instantaneous changes in the separation and orientation of the two components defined at t_0, for linearized orbital motion. We find that the orbit parameters are relatively poorly constrained, and we therefore restrict the MCMC trials to $\beta < 0.8$, where β is the ratio of projected kinetic to potential energy (Dong et al. 2009):

$$\beta \equiv \left| \frac{KE_\perp}{PE_\perp} \right| = \frac{\kappa\,M_\odot yr^{-2}}{8\pi^2} \frac{\pi_E}{\theta_E} \gamma^2 \left(\frac{s}{\pi_E + \pi_S/\theta_E} \right)^3; \quad \gamma \equiv \left(\frac{ds/dt}{s}, \frac{d\alpha}{dt} \right), (7)$$

and we adopt $\pi_S = 0.13$ mas for the source parallax, $\theta_* = 2.75\,\mu$as from Section 5.1 (and thus, $\theta_E = \theta_*/\rho$). We also fit $u_0 > 0$ and $u_0 < 0$ models to consider the 'ecliptic degeneracy' (Jiang et al. 2004; Poindexter et al. 2005). Table 3 displays the resultsing parameters. See the top panels of Fig. 6 for the error contours of annual parallax. For both $u_0 > 0$ and $u_0 < 0$ models, we find that the χ^2 improvement relative to the static model is only 1.5 and $\pi_{E,E}$ has a best-fitting value of ~ -0.3 with an 1σ error of 0.27. For the $u_0 > 0$ model, $\pi_{E,N}$ has an 1σ error of 0.15, while $\pi_{E,N}$ is only broadly constrained for the $u_0 < 0$ model. The effects of lens orbital motion is not detectable

($\Delta\chi^2 = 0.2$) and not significantly correlated with π_E, so we eliminate the lens orbital motion from the fit.[4]

4 PARALLAX ANALYSIS INCLUDING *Spitzer* DATA

Simultaneous observations from two widely separated observers can result in two different observed light curves (Refsdal 1966), which yields the measurement of the microlens parallax (see fig. 1 of Gould 1994):

$$\pi_E = \frac{AU}{D_\perp} (\Delta\tau, \Delta\beta), \tag{8}$$

with

$$\Delta\tau \equiv \frac{t_{0,Spitzer} - t_{0,\oplus}}{t_E}; \qquad \Delta\beta \equiv \pm u_{0,Spitzer} - \pm u_{0,\oplus}, \tag{9}$$

where $D_\perp$ is the projected separation between the *Spitzer* satellite and Earth at the time of the event. In addition, we include a *VIL* colour–colour constraint on the *Spitzer* source flux $f_{s,Spitzer}$ (e.g. Shin et al. 2018), which adds a χ^2_{penalty} into the total χ^2:

$$\chi^2_{\text{penalty}} = \frac{[(I-L)_S - (I-L)_{\text{fix}}]^2}{\sigma^2_{cc}}, \tag{10}$$

where $(I-L)_S$ is the source colour from the modelling, $(I-L)_{\text{fix}}$ is the colour constraint, and σ_{cc} is the uncertainty of the colour constraint. To derive the colour–colour constraint of the *Spitzer* source flux, we extract *Spitzer* and KMTC photometry for the stars within the range $1.8 < (V-I)_{\text{KMT}} < 2.5$, which have colour close to the source star. We obtain the colour–colour relation

$$I_{\text{KMT}} - L_{Spitzer} = 1.74 + [1.38(V-I)_{\text{KMT}} - 2.08]. \tag{11}$$

In Section 5, we find $(V-I)_{\text{KMT}} = 2.035 \pm 0.018$. Hence,

$$(I_{\text{KMT}} - L_{Spitzer})_{\text{fix}} = 1.678 \pm 0.026. \tag{12}$$

4.1 *Spitzer* systematics investigation and *Spitzer*-'ONLY' parallax

Poleski et al. (2016) were the first to discuss correlated noise in the *Spitzer* data, and Zhu et al. (2017b) found that the *Spitzer* data of six events have prominent deviations (see their fig. 6 for an example), which is likely due to systematics in the *Spitzer* data. Koshimoto & Bennett (2020) conducted a quantitative statistical test to the 50-event statistical sample of Zhu et al. (2017b) and found a conflict between the *Spitzer* microlensing parallax measurements and the predictions from Galactic models.

In order to check for the impact of systematic errors on the measured parallax, all known *Spitzer* planetary events from 2014–2018 were reobserved for about a week at baseline during the (final) 2019 season. Gould et al. (2020) first tested the *Spitzer* systematics using these baseline data for the event KMT-2018-BLG-0029. They divided the 2018 *Spitzer* data into two parts ('first-half-2018' and 'second-half-2018') and combined each part with the 2019 data, as well as discussing the results from 2018 data alone. They conclude that the 'second-half-2018' *Spitzer* data show clear residuals that are correlated in time, so should be excluded. Subsequently, in the event OGLE-2017-BLG-0406, Hirao et al. (2020) found a similar effect.

---

[4] We also check whether the constraint of lens orbital motion could be improved by including *Spitzer* data, but the constraint is still weak ($\Delta\chi^2 < 1$).
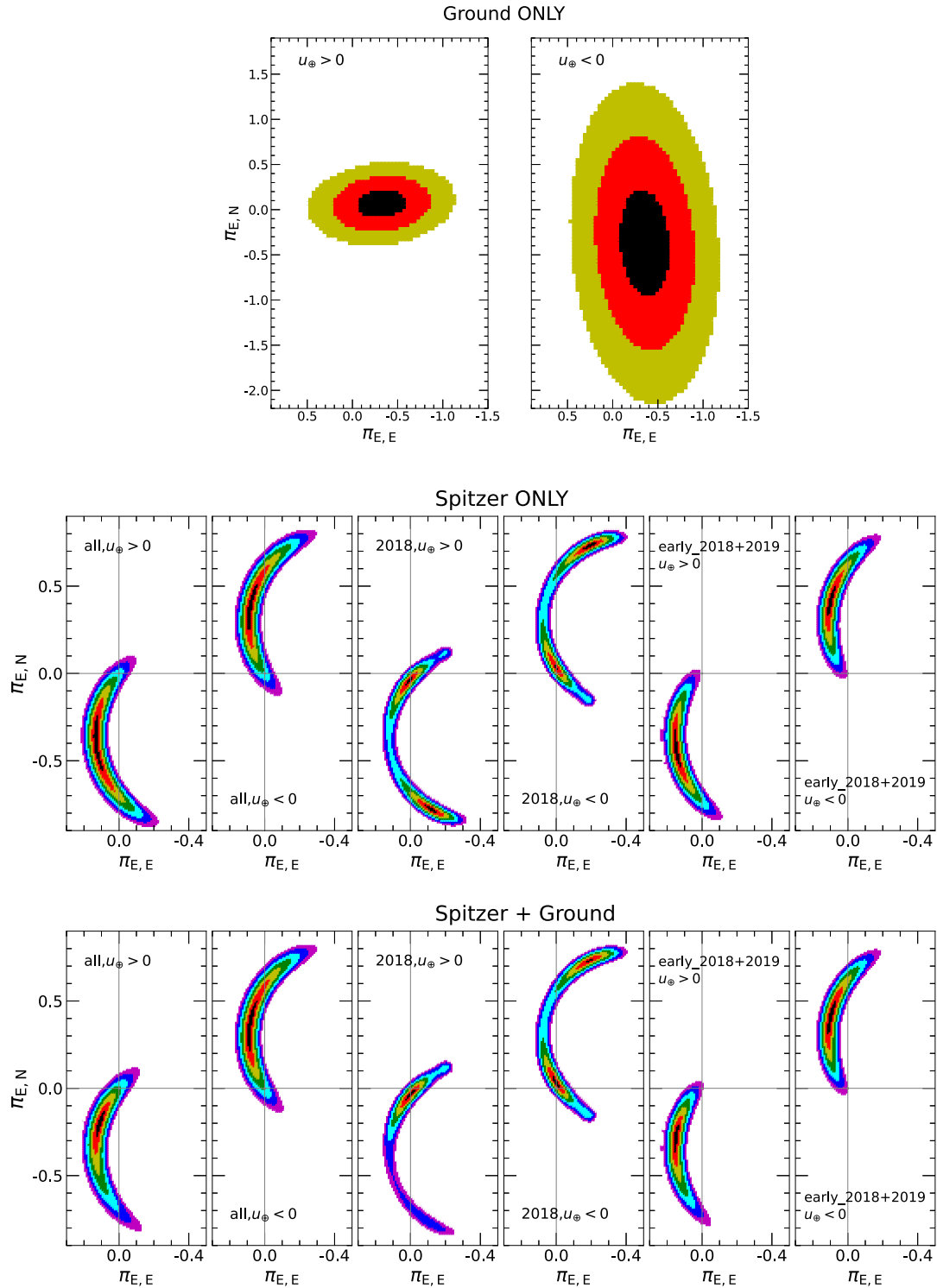
Figure 6. Parallax constraints from Ground-ONLY (top panels), *Spitzer*-'ONLY' (middle panels), and Ground + *Spitzer* (bottom panels) parallax analysis. Colours (black, red, yellow, green, cyan, blue, magenta) indicate number of σ from the minimum (1, 2, 3, 4, 5, 6, 7). From the left- to right-hand side for the middle and bottom panels, contours are shown for the full *Spitzer* data set, the 2018 data alone, and the first half of 2018 + the 2019 data (referred to as the 'early_2018 + 2019' subset in the text).

They analysed the *Spitzer* parallax with 2019 baseline data and found evidence of systematic errors in the last six *Spitzer* data points from 2017. They repeated the analysis with and without those six points and show that they only affect the *Spitzer* parallax measurements at less than 1σ. Furthermore, they discuss the effects on resulting

parallax contours in the context of the Gould (2019) osculating circles formalism. In these two cases, the subsets of *Spitzer* data with clear systematic errors are in the second half of the *Spitzer* observing season. Because the observing conditions (such as the rotation of the spacecraft or angle with the Sun) change over the course of a given

Table 3. Parallax models for the solution A for ground-only data.

	$u_0 > 0$		$u_0 < 0$	
Models	Parallax	Parallax + Orbit	Parallax	Parallax + Orbit
χ^2/d.o.f.	1703.3/1703	1703.1/1701	1703.3/1703	1703.1/1701
t_0 (HJD$'$)	8295.16 ± 0.02	8295.15 ± 0.03	8295.15 ± 0.02	8295.16 ± 0.04
u_0	0.413 ± 0.012	0.419 ± 0.015	-0.417 ± 0.013	-0.418 ± 0.014
t_E (d)	27.7 ± 0.6	27.5 ± 0.7	27.5 ± 0.6	27.5 ± 0.7
s	1.123 ± 0.012	1.128 ± 0.024	1.127 ± 0.012	1.128 ± 0.025
$q(10^{-3})$	2.61 ± 0.16	2.52 ± 0.49	2.58 ± 0.17	2.61 ± 0.77
α (rad)	1.173 ± 0.003	1.175 ± 0.004	-1.175 ± 0.003	-1.181 ± 0.004
ρ	<0.024	<0.025	<0.025	<0.025
$\pi_{E,N}$	0.076 ± 0.154	0.097 ± 0.164	-0.366 ± 0.592	-0.798 ± 0.720
$\pi_{E,E}$	-0.317 ± 0.272	-0.425 ± 0.307	-0.354 ± 0.275	-0.399 ± 0.317
ds/dt (yr^{-1})	...	0.058 ± 0.943	...	0.546 ± 0.981
dα/dt (yr^{-1})	...	0.103 ± 2.575	...	0.340 ± 4.790
$f_{S,\,OGLE}$	1.886 ± 0.080	1.897 ± 0.097	1.905 ± 0.082	1.894 ± 0.094
$f_{B,\,OGLE}$	-0.128 ± 0.081	-0.139 ± 0.099	-0.146 ± 0.084	-0.135 ± 0.096

Notes. The values of ρ are their 3σ upper limits. All fluxes are on an 18th magnitude scale, e.g. $I_S = 18 - 2.5\log(f_S)$. Ellipses means that the parameter is not included in the model.

season, the first half of the data from each season has more similar observing conditions to the 2019 baseline data, which were taken at the beginning of the 2019 season.

We follow the established procedure of Gould et al. (2020) and Hirao et al. (2020) to investigate the potential *Spitzer* systematics for OGLE-2018-BLG-0799. We perform this analysis on both the full *Spitzer* data set ('all') and two subsets of the data ('2018' and 'early_2018 + 2019').

For the '2018' subset, we use only data taken in 2018, and we exclude the 2019 baseline observations. This data set matches what would be used for a 'normal' *Spitzer* event. Thus, for the statistical sample, membership in that sample should be determined solely on the basis of these data.

Following the method of Gould et al. (2020), we also fit just the first half (HJD$'$ < 8326) of the 2018 *Spitzer* data combined with the 2019 baseline data (i.e. the 'early_2018 + 2019' subset). As discussed in Gould et al. (2020), because the 2019 data were taken near the beginning of the 2019 observing window, the observing conditions are more similar at the beginning of the 2018 observing window.

In order to isolate the satellite parallax signal due to *Spitzer's* separation from Earth, we first fit for the *Spitzer*-'ONLY' parallax (Jung et al. 2019). We fix $(t_0, u_0, t_E, s, q, \alpha, \rho)$ along with the KMTC source flux as the best-fitting parameters for the ground-based static models (shown in Table 2), and then fit $(\pi_{E,N}, \pi_{E,E}, f_{S,\,Spitzer}, f_{B,\,Spitzer})$ with the derived *VIL* colour–colour constraint (equation 12). We repeat the analysis for both the $u_0 > 0$ and $u_0 < 0$ solutions.

The error contours for the parallax vector derived from this analysis are shown in the middle panels of Fig. 6. Although the χ^2 contours have a similar arc-like form in all three cases, the measured value of the parallax and the 3σ uncertainties are disjoint (or close to disjoint) for the '2018' subset of the data as compared to the subsets including the 2019 baseline data. Because Gould et al. (2020) and Hirao et al. (2020) have shown that results of the subset with similar observing conditions are the least likely to be affected by the *Spitzer* systematics, we adopt the results for the 'early_2018 + 2019' subset as our fiducial values. Indeed, adding the second half of the 2018 data, i.e. using all the data, stretches the contours towards the 2018-only result rather than refining them, indicating some effects from systematics. We discuss the implications of these discrepancies in detail in Sections 5 and 6.

4.2 Full parallax models

We finally fit the parallax combining ground-based and *Spitzer* data together. The resulting parallax contours are shown in the bottom panels of Fig. 6, and the resulting parameters are shown in Table 4. There is some tension between the annual parallax constrained by ground-based data alone and the parallax measured from the *Spitzer* light curve. In particular, the annual parallax prefers a negative value of $\pi_{E,E}$ (~-0.3), whereas the *Spitzer*-'ONLY' parallax prefers a positive value of $\pi_{E,E}$ (~0.1) when the 2019 baseline data are included. The tension with the annual parallax suggests the constraint is driven by some systematics in the ground-based data or stellar variability of the source star. However, we were unable to definitively identify the cause of the discrepancy or source of the systematics. Regardless, because the constraints from the annual parallax are broad, when the two effects are combined, the final result is dominated by the *Spitzer* parallax.

5 PHYSICAL PROPERTIES

Our physical interpretation of the lens is substantially different with and without the 2019 *Spitzer* baseline data. To simplify the discussion and show how the problem derives primarily from the parallax measurement itself, we begin in Section 5.1 by estimating the angular source radius θ_* and the angular Einstein radius θ_E. Then, in Section 5.2, we examine the constraints on the lens mass M_L and distance D_L derived directly from θ_E and $|\pi_E|$. Finally, in Section 5.3, we carry out a full Bayesian analysis to derive the properties of the lens weighted by a Galactic model.

5.1 Colour–magnitude diagram

The angular Einstein radius $\theta_E = \theta_*/\rho$. Thus, we estimate θ_* using a CMD analysis (Yoo et al. 2004). We construct a KMTC $V - I$ versus I CMD using stars within a 120 arcsec^2 centred on the source position (see Fig. 7). We measure the centroid of the red clump $(V - I, I)_{cl} = (2.09 \pm 0.01, 15.83 \pm 0.04)$. We determine the source colour by regression of V versus I flux as the source magnification changes, and find the source position $(V - I, I)_S = (2.035 \pm 0.018, 17.46 \pm 0.03)$. From Bensby et al. (2013) and Nataf et al. (2013), the intrinsic colour and de-reddened brightness of the red clump are $(V - I, I)_{cl,0} = (1.06, 14.27)$. Assuming the source suffers from the same dust extinction

Table 4. Best-fitting models and their 68 per cent uncertainty ranges from MCMC for full parallax models.

Models	'all'		'2018'		'early_2018 + 2019'	
Parameters	$u_{0,\oplus} > 0$	$u_{0,\oplus} < 0$	$u_{0,\oplus} > 0$	$u_{0,\oplus} < 0$	$u_{0,\oplus} > 0$	$u_{0,\oplus} < 0$
χ^2_{total}/d.o.f.	1744.5/1737	1742.1/1737	1734.1/1732	1734.3/1732	1729.9/1722	1726.5/1722
t_0 (HJD$'$)	8295.13 ± 0.02	8295.13 ± 0.02	8295.13 ± 0.02	8295.15 ± 0.02	8295.13 ± 0.02	8295.13 ± 0.02
$u_{0,\oplus}$	0.400 ± 0.009	-0.402 ± 0.009	0.401 ± 0.010	-0.404 ± 0.010	0.399 ± 0.009	-0.403 ± 0.009
t_E (d)	28.4 ± 0.4	28.2 ± 0.4	28.3 ± 0.4	28.1 ± 0.4	28.4 ± 0.4	28.2 ± 0.4
s	1.111 ± 0.009	1.114 ± 0.009	1.115 ± 0.009	1.116 ± 0.009	1.112 ± 0.009	1.117 ± 0.009
$q(10^{-3})$	2.70 ± 0.16	2.70 ± 0.16	2.62 ± 0.16	2.65 ± 0.16	2.65 ± 0.16	2.64 ± 0.16
α (rad)	1.168 ± 0.003	1.169 ± 0.003	1.167 ± 0.003	-1.170 ± 0.003	1.167 ± 0.003	-1.169 ± 0.003
ρ	<0.026	<0.026	<0.026	<0.026	<0.026	<0.026
$\pi_{E,N}$	-0.218 ± 0.082	0.373 ± 0.126	-0.037 ± 0.034	0.047 ± 0.043	-0.301 ± 0.077	0.410 ± 0.090
$\pi_{E,E}$	0.121 ± 0.021	0.083 ± 0.030	0.006 ± 0.027	-0.020 ± 0.025	0.152 ± 0.012	0.109 ± 0.023
$f_{S,\ OGLE}$	1.771 ± 0.053	1.790 ± 0.053	1.781 ± 0.053	1.802 ± 0.053	1.769 ± 0.052	1.747 ± 0.053
$f_{B,\ OGLE}$	-0.007 ± 0.052	-0.025 ± 0.052	-0.018 ± 0.052	-0.039 ± 0.052	-0.004 ± 0.051	0.017 ± 0.052
$f_{S,\ Spitzer}$	7.633 ± 0.296	7.815 ± 0.297	7.818 ± 0.293	7.928 ± 0.294	7.671 ± 0.289	7.523 ± 0.293
$f_{B,\ Spitzer}$	-0.162 ± 0.294	-0.334 ± 0.294	-0.783 ± 0.305	-0.872 ± 0.302	0.125 ± 0.287	0.267 ± 0.290
$\chi^2_{penalty}$	0.265	0.001	0.070	0.122	0.065	0.053

Note. From the left- to right-hand side, parameters are shown for the full *Spitzer* data set ('all'), the 2018 data alone ('2018'), and the first half of 2018 + the 2019 data ('early_2018 + 2019'). The values of ρ are their 3σ upper limits. All fluxes are on an 18th magnitude scale, e.g. $L_{S,\ Spitzer} = 18 - 2.5\log(f_{S,\ Spitzer})$.

Table 5. Physical parameters from Bayesian analysis.

		Physical properties						Relative weights	
Data set	Solutions	$M_{host}(M_\odot)$	$M_{planet}(M_J)$	D_L(kpc)	$r_\perp$(AU)	$\mu_{hel,rel}$(mas yr^{-1})	P_{bulge}	Gal. mod.	χ^2
'all'	$u_{0,\oplus} > 0$	$0.14^{+0.11}_{-0.05}$	$0.38^{+0.31}_{-0.14}$	$6.58^{+0.50}_{-0.48}$	$1.19^{+0.33}_{-0.21}$	$2.13^{+0.62}_{-0.38}$	0.979	0.728	0.301
	$u_{0,\oplus} < 0$	$0.13^{+0.12}_{-0.06}$	$0.37^{+0.35}_{-0.17}$	$5.29^{+1.30}_{-1.82}$	$1.34^{+0.65}_{-0.35}$	$2.97^{+3.52}_{-1.06}$	0.395	1.000	1.000
	Combined	$0.13^{+0.12}_{-0.05}$	$0.38^{+0.32}_{-0.16}$	$6.28^{+0.64}_{-2.02}$	$1.24^{+0.52}_{-0.26}$	$2.33^{+2.22}_{-0.52}$	0.500	...	...
'2018'	$u_{0,\oplus} > 0$	$0.62^{+0.25}_{-0.25}$	$1.68^{+0.68}_{-0.68}$	$7.14^{+0.50}_{-0.50}$	$1.41^{+0.49}_{-0.29}$	$2.27^{+0.82}_{-0.46}$	0.979	0.733	1.000
	$u_{0,\oplus} < 0$	$0.59^{+0.27}_{-0.26}$	$1.62^{+0.72}_{-0.71}$	$7.06^{+0.54}_{-0.56}$	$1.45^{+0.59}_{-0.32}$	$2.35^{+1.04}_{-0.52}$	0.896	1.000	0.905
	Combined	$0.60^{+0.26}_{-0.26}$	$1.65^{+0.71}_{-0.70}$	$7.10^{+0.52}_{-0.54}$	$1.43^{+0.55}_{-0.31}$	$2.31^{+0.94}_{-0.48}$	0.933	...	...
'early_2018 + 2019'	$u_{0,\oplus} > 0$	$0.074^{+0.030}_{-0.020}$	$0.21^{+0.08}_{-0.06}$	$6.19^{+0.47}_{-0.43}$	$1.02^{+0.20}_{-0.15}$	$1.95^{+0.42}_{-0.28}$	0.980	0.367	0.183
	$u_{0,\oplus} < 0$	$0.096^{+0.083}_{-0.040}$	$0.27^{+0.23}_{-0.12}$	$3.93^{+3.16}_{-1.84}$	$1.31^{+0.47}_{-0.36}$	$3.93^{+3.16}_{-1.84}$	0.147	1.000	1.000
	Combined	$0.093^{+0.082}_{-0.038}$	$0.26^{+0.22}_{-0.11}$	$4.05^{+1.78}_{-1.16}$	$1.28^{+0.48}_{-0.34}$	$3.71^{+3.24}_{-1.70}$	0.199	...	...

Notes. P_{bulge} is the probability of a lens in the Galactic bulge. The combined result of each *Spitzer* data set is obtained by a combination of $u_{0,\oplus} > 0$ and $u_{0,\oplus} < 0$ solutions weighted by the probability for the Galactic model and $\exp(-\Delta\chi^2/2)$. Ellipses means that the combined solutions do not contain the weights.

as the red clump, the intrinsic colour and de-reddened magnitude of the source are $(V - I, I)_{S,0} = (1.00 \pm 0.03, 15.90 \pm 0.05)$. Using the colour/surface–brightness relation of Adams, Boyajian & von Braun (2018), we obtain

$$\theta_* = 2.75 \pm 0.20\ \mu as. \tag{13}$$

By itself, the 3σ upper limit from ρ alone yields a lower limit on the angular Einstein radius of $\theta_E > 0.106$ mas. However, there is, in fact a preferred value of ρ from the fitting. Thus, combining the probability distribution function for ρ from the full parallax models with θ_*, yields a probability distribution of θ_E, which is shown in Fig. 8.

5.2 Approximate

From the microlensing light curve, the ground-based data give a constraint on θ_E and the *Spitzer* data give a measurement of $|\pi_E|$. Each of θ_E and $|\pi_E|$ yields a mass–distance relationship (equations 1 and 2) as shown in the left-hand panels of Fig. 9. For the $|\pi_E|$ constraint, we used the minimum χ^2 for a given radius π_E from the contours shown in Fig. 6. For simplicity, we focus this discussion on the $u_0 < 0$ solution and the parallaxes derived from the 'early_2018

+ 2019' and '2018' subsets of the *Spitzer* data (the similarity in the parallax contours means that the $u_0 > 0$ solution and/or full *Spitzer* data set yield qualitatively similar results). The θ_E relation is the same in all cases. The 1σ, 2σ, and 3σ limits for this relation are derived from the probability distribution shown in Fig. 8.

The 'early_2018 + 2019' case yields the simple intersection of two relations, but the '2018' case yields bimodal values for the parallax and hence, a pair of intersections with the θ_E constraint. However, we can also take into account the fact that more distant lenses are more likely, because the volume of stars is larger at larger distances for fixed θ_E. Thus, we sum the χ^2s from the two constraints and weight by a factor of D_L^2 to produce 1σ, 2σ, and 3σ contours for the lens mass and distance (right-hand panels of Fig. 9). This down-weights the smaller D_L minimum (corresponding to the parallax minimum with larger $|\pi_E|$) in the '2018' case. Finally, we find for the 'early_2018 + 2019' case that the lens primary is a VLM object. In contrast, the 2018 data alone suggest that the lens is likely to be a K or G dwarf. Adding the additional priors for a full Bayesian analysis will alter the details of these contours but does not change the underlying discrepancy in the lens interpretation, which ultimately derives from the differences in the parallax contours.
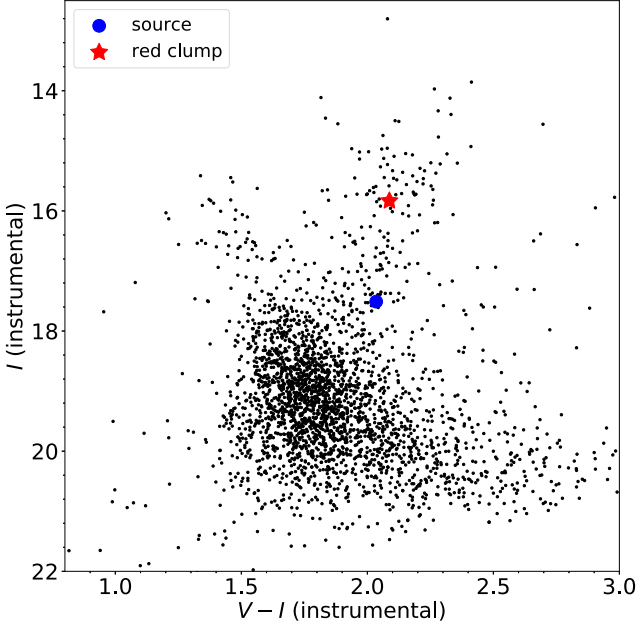
Figure 7. Instrumental CMD of a 120 arcsec^2 centred on OGLE-2018-BLG-0799 using KMTC data. The red asterisk and blue dot represent the centroid of the red clump and the position of the microlens source, respectively.
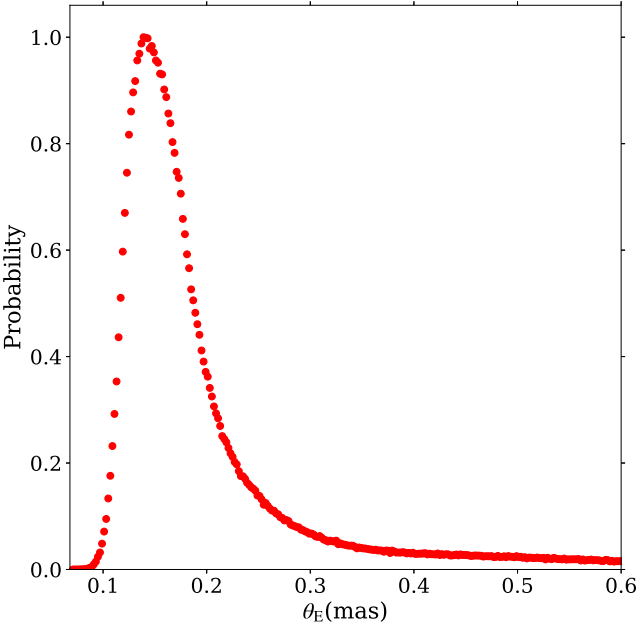
Figure 8. Probability distributions of the angular Einstein radius θ_E, which is estimated by $\theta_E = \theta_*/\rho$. We obtain θ_* by CMD analysis (see Section 5.1), and ρ is derived from the minimum χ^2 for the lower envelope of the (χ^2 versus ρ) diagram from MCMC chain of full parallax models. $\theta_E = 0.14$ mas is the most likely value and $\theta_E > 0.092$ mas at 3σ level, but the upper limit on θ_E is not constrained at the 2.7σ level.

5.3 Bayesian analysis

We perform a Bayesian analysis using a Galactic model based on the mass function, stellar number density profile, and the source and lens velocity distributions. For the mass function of the lens, we choose the lognormal initial mass function of Chabrier (2003) and impose cut offs of 1.3 (Zhu et al. 2017b) and 1.1 M$_\odot$ (Bensby

et al. 2017) for the disc lenses and bulge lenses, respectively. For the bulge and disc stellar number density profile, we choose the model used by Zhu et al. (2017b) and Bennett et al. (2014), respectively. For the source velocity distribution, we adopt the source proper motion measured by *Gaia* (Gaia Collaboration et al. 2016, 2018):

$$\boldsymbol{\mu}_\mathrm{S}(N, E) = (-6.17 \pm 0.66, 0.54 \pm 0.74) \ \mathrm{mas\ yr}^{-1}. \tag{14}$$

For the velocity distribution of the lens in the Galactic bulge, we examine a *Gaia* CMD using the stars within 5 arcmin and derive the proper motion (in the Sun frame) for stars with $G < 18.5$; $B_p - R_p > 1.5$. We remove seven outliers and obtain

$$\langle \boldsymbol{\mu}_\mathrm{bulge}(\ell, b) \rangle = (-5.9, -0.6) \pm (0.4, 0.3) \ \mathrm{mas\ yr}^{-1}, \tag{15}$$

$$\sigma(\boldsymbol{\mu}_\mathrm{bulge}) = (2.7, 2.8) \pm (0.3, 0.3) \ \mathrm{mas\ yr}^{-1}. \tag{16}$$

Assuming the source distance is 7.55 kpc (inferred from the de-reddened brightness of the red clump $I_\mathrm{cl} = 14.27$), the bulge stars toward this direction have mean velocity $\boldsymbol{v}(\ell, b) \sim (40, -10) \ \mathrm{km\ s}^{-1}$ and $\sigma_v \sim 100 \ \mathrm{km\ s}^{-1}$ velocity dispersion along each direction. For the disc lens velocity distribution, we assume the disc stars follow a rotation curve of 240 km s^{-1} (Reid et al. 2014) and adopt the velocity dispersion of Han et al. (2020).

We create a sample of 2×10^9 simulated events and weight the six full parallax models shown in Table 4. For each simulated event i of model k, the weight is given by

$$W_{\mathrm{Gal},i,k} = \Gamma_{i,k} \mathcal{L}_{i,k}(t_E) \mathcal{L}_{i,k}(\pi_E) \mathcal{L}_{i,k}(\theta_E), \tag{17}$$

where $\Gamma_{i,k} \propto \theta_{E,i,k} \times \mu_{\mathrm{rel},i,k} \times D_L^2$ is the microlensing event rate, $\mathcal{L}_{i,k}(\pi_E)$ and $\mathcal{L}_{i,k}(\theta_E)$ are the likelihood distribution for π_E and θ_E shown in Figs 6 and 8, respectively, and $\mathcal{L}_{i,k}(t_E)$ are the likelihood of its inferred parameters $t_{E,i,k}$, given the error distributions of these quantities derived from the MCMC for that model:

$$\mathcal{L}_{i,k}(t_E) = \frac{\exp\left[-(t_{E,i,k} - t_{E,k})^2/2\sigma_{t_{E,k}}^2\right]}{\sqrt{2\pi}\sigma_{t_{E,k}}}. \tag{18}$$

For each data set, we weight each solution by its probability for the Galactic model and $\exp(-\Delta\chi^2/2)$, where $\Delta\chi^2$ is the χ^2 difference between the solution and the best-fitting solution. In addition, the blended light is consistent with zero in 1σ (see Table 4), which can a provide useful constraint on the lens flux. We adopt 10 per cent of the source flux as the upper limit of the lens flux, $I_{\mathrm{L,limit}} = 19.9$, which is roughly the 3σ upper limit of the blended light. We then adopt the mass–luminosity relation of Wang et al. (2018):

$$M_I = 4.4 - 8.5 \log\left(\frac{M_L}{M_\odot}\right), \tag{19}$$

where M_I is the absolute magnitude in the I band, and reject trial events for which the lens properties obey

$$M_I + 5\log\frac{D_L}{10\mathrm{pc}} + A_{I,D_L} < I_{\mathrm{L,limit}}, \tag{20}$$

where A_{I,D_L} is the extinction at D_L, which is derived by an extinction curve with a scaleheight of 120 pc and $A_{I,7.55\,\mathrm{kpc}} = 1.29$ from Nataf et al. (2013).

The distributions and relative weights for each solution and the combined results are shown in Table 5. For each solution, the resulting distributions of the lens host-mass M_host and the lens distance D_L are shown in Fig. 10. The physical properties for the lens are different for different subsets of the *Spitzer* data. For 'all'
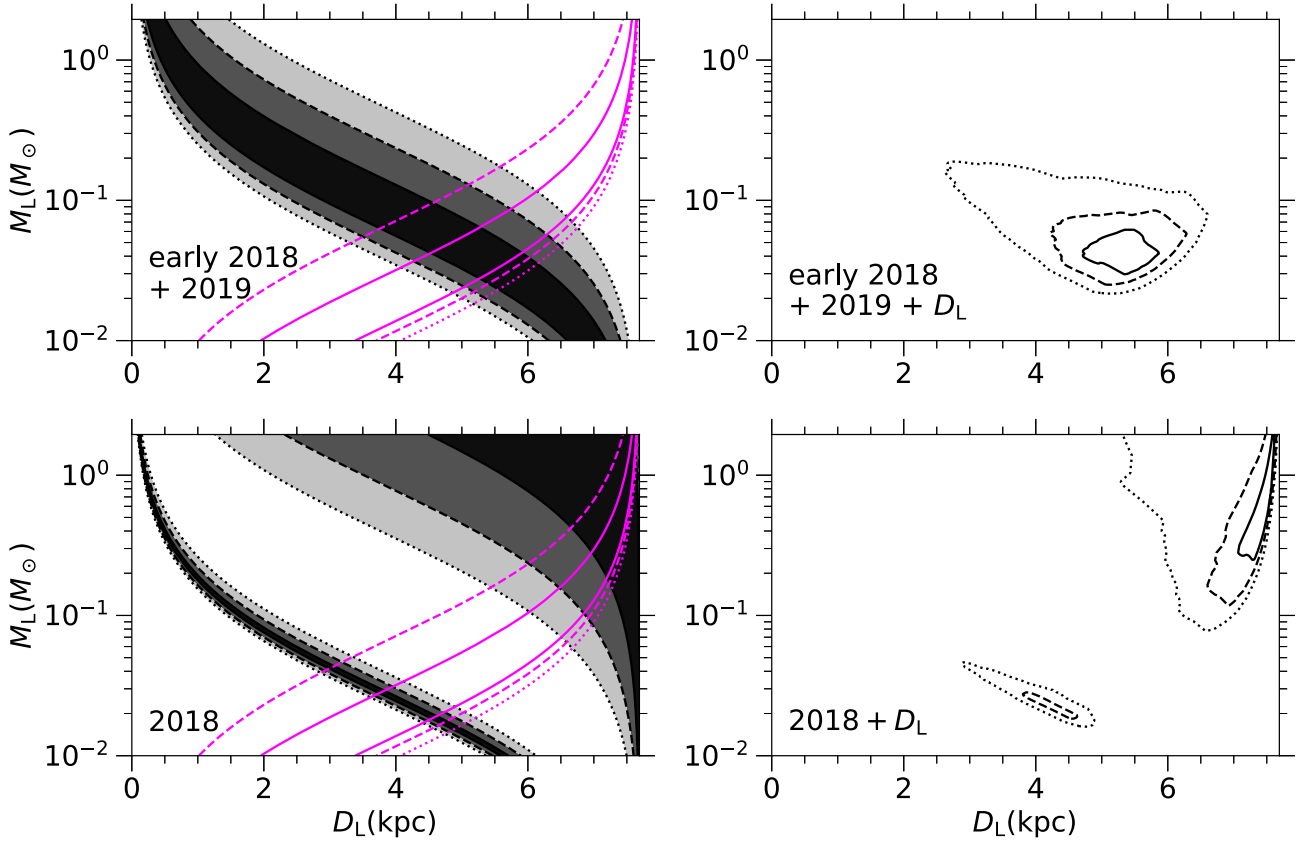
Figure 9. Constraints on the lens mass and system distance for OGLE-2018-BLG-0799. Left-hand panel: 1σ, 2σ, and 3σ (solid, dashed, dotted) constraints from the angular Einstein radius θ_E (magenta) and the microlens parallax $|\pi_E|$ (black/shaded). Right-hand panel: the joint constraint weighted by a factor D_L^2. Top panel: parallax constraint derived from the first half of the 2018 *Spitzer* data + the 2019 baseline observations ('early_2018 + 2019'). Bottom panel: parallax constraint derived from all 2018 *Spitzer* data but excluding the 2019 observations.

Spitzer data, the Bayesian analysis indicates that the lens system is composed of an $M_{planet} = 0.38^{+0.32}_{-0.16} M_J$ sub-Jupiter orbiting an $M_{host} = 0.13^{+0.12}_{-0.05}$ M$_\odot$ M dwarf or brown dwarf, the 'early_2018 + 2019' subset suggests an $M_{planet} = 0.26^{+0.22}_{-0.11} M_J$ Saturn around an $M_{host} = 0.093^{+0.082}_{-0.038}$ M$_\odot$ VLM dwarf, and the '2018' subset indicates an $M_{planet} = 1.65^{+0.71}_{-0.70} M_J$ Jupiter orbiting an $M_{host} = 0.60^{+0.26}_{-0.26}$ M$_\odot$ more massive dwarf. The 'early_2018 + 2019' subset prefers a disc planetary system, the '2018' subset prefers a bulge planetary system, and the 'all' subset has an equal probability of a bulge or a disc system.

6 IMPLICATIONS

The difference between the parallax contours with and without the 2019 *Spitzer* baseline observations presents two problems. First, it complicates our interpretation of OGLE-2018-BLG-0799 because the different parallaxes result in radically different physical properties for the lens. Secondly, it is unclear whether or not this planet can be included in the statistical *Spitzer* sample for measuring the frequency of planets.

The goal of the *Spitzer* microlensing program is to create a statistical sample of events (including planets) with well-measured distances in order to probe variations in the frequency of planets along the line of sight. Previously, Zhu et al. (2017b) proposed that events should have

$$\sigma(D_{8.3}) < 1.4 \text{ kpc}; \qquad D_{8.3} \equiv \frac{\text{kpc}}{1/8.3 + \pi_{rel}/\text{mas}} \qquad (21)$$

to be included in the sample. For a planetary event, $\sigma(D_{8.3})$ should be evaluated based on data from which the planet has been removed and only including *Spitzer* data scheduled without knowledge of the planet (so that the event can be evaluated under the same conditions as events without planets). We follow the procedures described in Ryu et al. (2018) to fit with a point-lens model using the analogous data and conduct a Bayesian analysis without the constraint of the finite-source effects. We find $D_{8.3} = 3.72^{+1.42}_{-1.00}$ kpc for the 'all' *Spitzer* data, $D_{8.3} = 7.40^{+0.45}_{-0.81}$ kpc for the '2018' subset, and $D_{8.3} = 3.09^{+0.91}_{-0.79}$ kpc for the 'early_2018 + 2019' subset. So $D_{8.3}$ is constrained well enough at 1σ to meet the Zhu et al. (2017b) criterion in two of three cases, and especially in the '2018' case by which the criterion should be evaluated. However, the parallax as measured from the 2018 *Spitzer* data alone is different from the parallax based on an analysis including the 2019 *Spitzer* baseline data. Furthermore, in the case with 'all' data, the constraints on $D_{8.3}$ are worse and fail the criterion. This suggests that we may need to re-evaluate how we interpret parallaxes measured from *Spitzer* light curves and also how the statistical sample of *Spitzer* events is defined.

The change in the parallax contours with the addition of 2019 *Spitzer* baseline observations indicate that systematics in the photometry are affecting the parallax constraint. Some level of systematics (or rather correlated noise) has always been present in the *Spitzer* photometry of microlensing events (e.g. Poleski et al. 2016). As noted in Zhu et al. (2017b), there are several examples of cases for which the annual parallax effect confirms the satellite parallax effect (Udalski et al. 2015b; Han et al. 2017). Hence, Zhu et al. (2017b) concluded
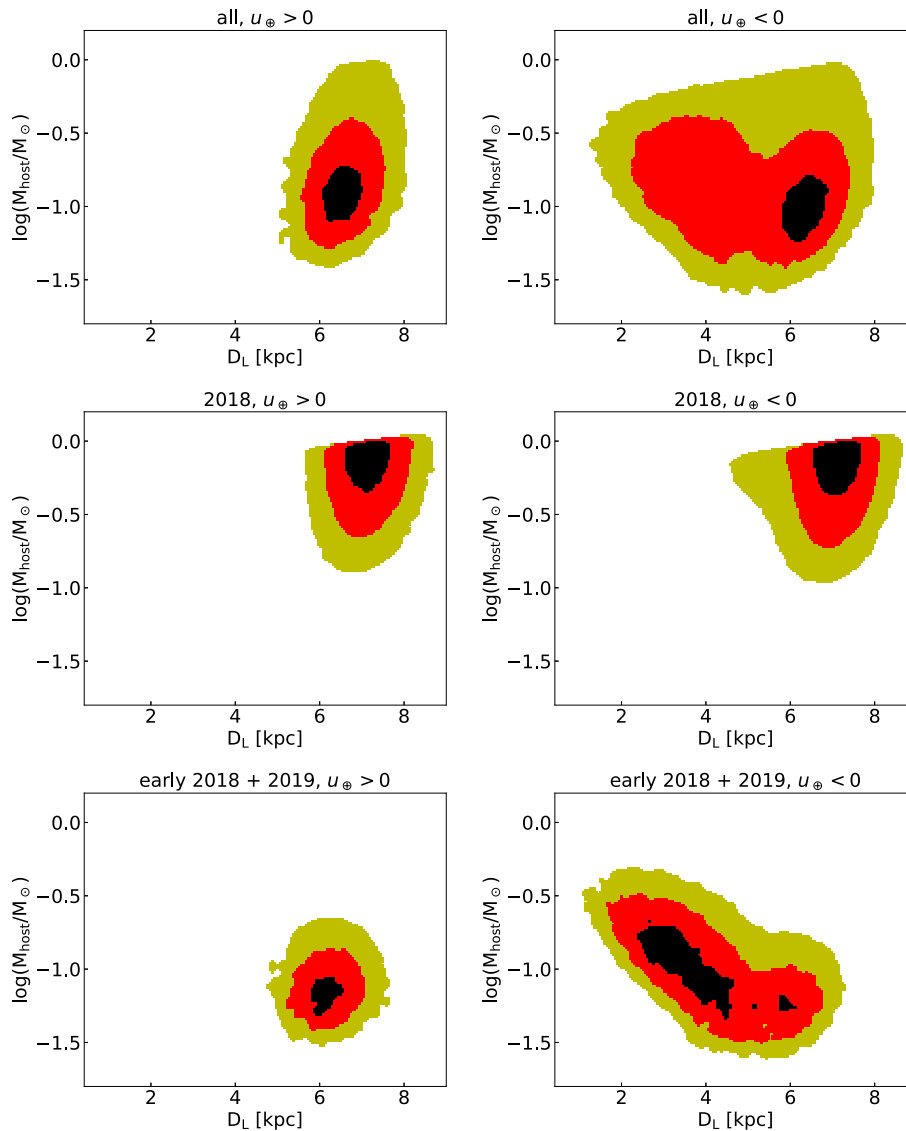
Figure 10. Bayesian posteriors distributions of the lens host-mass M_{host} and the lens distance D_L. In each panel, black, red, and yellow colours show likelihood ratios $[-2\Delta \ln \mathcal{L}/\mathcal{L}_{max}] < (1, 4, 9)$, respectively.

that these systematics do not have a significant effect on the resulting parallax measurements. By contrast, Koshimoto & Bennett (2020) compared the parallaxes measured for the Zhu et al. (2017b) sample to a predicted distribution of parallaxes from a galactic model. Based on the differences between the observed parallaxes and their prediction, they concluded that systematics caused *Spitzer* parallaxes to be overestimated. However, they did not investigate the actual *Spitzer* photometry.

OGLE-2018-BLG-0799 shows that, for at least some events, systematics in the photometry does play a significant role in the measured parallaxes. Thus, this issue requires a more systematic investigation of the photometry (and the resulting constraints on the parallax) in order to understand how often systematics in the photometry affect the measured parallax, the conditions under which those problems appear, and how the parallax measurement is affected.

The arc-like form of the parallax contours in OGLE-2018-BLG-0799 suggests the work of Gould (2019) can offer a deeper understanding of how to robustly assess the satellite parallaxes in the presence of photometric systematics. The development of the *Spitzer*-

'ONLY' method for investigating the satellite parallax has shown that the uncertainty contours for the parallax measured in the $\pi_{E, E}-\pi_{E, N}$ plane are frequently arc-shaped rather than simple ellipses (Shin et al. 2018; Jung et al. 2019; Gould et al. 2020; Zang et al. 2020a,b; Hirao et al. 2020). Gould (2019) then showed the theoretical origin of these arcs. Given a colour-constraint and a measurement of the baseline flux, each *Spitzer* observation yields a circular constraint on the parallax. Then, when combined, a group of late-time observations yields a series of osculating circles whose intersection defines the measurement of the parallax.

A partial ring (as would be created by a series of osculating circles) is exactly the form of the constraint that we see for OGLE-2018-BLG-0799. This suggests that the 2018 data alone give a good measurement of the resulting arc, but the systematics in this event lead to the wrong localization along this arc. Future investigations of the influence of systematics in *Spitzer* photometry on the measured parallaxes should focus on further understanding at these arc-like constraints and their relationship to the osculating circles of Gould (2019). In addition, the criterion for assessing membership in the

statistical *Spitzer* sample may need to be revised to account for these arcs and the two-dimensional nature of the parallax constraints.

7 CONCLUSION

In this paper, we have reported the discovery and analysis of the *Spitzer* microlens planet OGLE-2018-BLG-0799Lb. The mass ratio between the lens star and its companion is $q = (2.65 \pm 0.16) \times 10^{-3}$. The combined constraints from θ_E and π_E suggest that the host star is most likely to be a VLM dwarf. In our preferred solution using the subset of the *Spitzer* data from 'early_2018 + 2019', a full Bayesian analysis indicates that the planetary system is composed of a $M_{planet} = 0.26^{+0.22}_{-0.11} M_J$ planet orbiting a $M_{host} = 0.093^{+0.082}_{-0.038}$ M$_\odot$ dwarf, with a host-planet projected planet separation $r_\perp = 1.28^{+0.48}_{-0.34}$ AU, which indicates that the planet is a Saturn-mass planet beyond the snow line of a VLM dwarf (assuming a snow line radius $r_{SL} = 2.7(M/M_\odot)$ AU, Kennedy & Kenyon 2008). However, because of systematics in the *Spitzer* photometry, there is ambiguity in the parallax measurement. Using all of the *Spitzer* data yield a parallax that implies $M_{host} = 0.13^{+0.12}_{-0.05}$ M$_\odot$ at $D_L = 6.28^{+0.64}_{-2.02}$ kpc. Although we consider a VLM object in the disc to be the most likely explanation for the host star, it is also possible for it to be a more massive star in the Galactic bulge. Indeed, in the absence of the 2019 data, we would have concluded $M_{host} = 0.60^{+0.26}_{-0.26}$ at $D_L = 7.10^{+0.52}_{-0.54}$ kpc.

An adaptive optics measurement of (or constraint on) the lens flux would substantially improve the constraints on the lens and distinguish between the different parallax solutions. A strong upper limit on the flux could immediately rule out the 2018-only solution, and a detection would be constraining although some ambiguities may persist due to potential confusion with other stars. Furthermore, if one waited until the lens and source could be separately resolved (e.g. Bhattacharya et al. 2020), if the lens were detected, this would yield a measurement of the lens-source relative proper motion vector, $\boldsymbol{\mu_{rel}}$. Its magnitude, $|\boldsymbol{\mu_{rel}}|$, would give a measurement of θ_E, which is only constrained by the microlensing light curve. In addition, a measurement of $\hat{\boldsymbol{\mu}}_{rel} = \hat{\pi}_E$ would further constrain the parallax contours (e.g. Zang et al. 2020b), both improving the measurement of π_E and independently testing the impact of systematics in the *Spitzer* photometry. The lens-source relative proper motion in this event is slow ($\mu_{rel} \sim 3$ mas yr^{-1}), but such a measurement could be made in $\sim$20 yr with an 8–10 m class telescope if the lens is luminous or at first light of AO imagers on 30-m telescopes (or possibly with *JWST*) if the lens is a faint brown dwarf.

DATA AVAILABILITY

Data used in the light-curve analysis are provided along with publication.

REFERENCES

Adams A. D., Boyajian T. S., von Braun K., 2018, MNRAS, 473, 3608
Alard C., Lupton R. H., 1998, ApJ, 503, 325
Albrow M. D. et al., 2009, MNRAS, 397, 2099
Alcock C. et al., 2001, Nature, 414, 617
An J. H. et al., 2002, ApJ, 572, 521
Batista V., Beaulieu J.-P., Bennett D. P., Gould A., Marquette J.-B., Fukui A., Bhattacharya A., 2015, ApJ, 808, 170
Beaulieu J. P. et al., 2018, AJ, 155, 78
Bennett D. P. et al., 2008, ApJ, 684, 663
Bennett D. P. et al., 2010, ApJ, 713, 837
Bennett D. P. et al., 2014, ApJ, 785, 155
Bennett D. P. et al., 2015, ApJ, 808, 169
Bennett D. P. et al., 2020, AJ, 159, 68
Bensby T. et al., 2013, A&A, 549, A147
Bensby T. et al., 2017, A&A, 605, A89
Bhattacharya A. et al., 2018, AJ, 156, 289
Bhattacharya A. et al., 2020, preprint (arXiv:2009.02329)
Bond I. A. et al., 2001, MNRAS, 327, 868
Bond I. A. et al., 2017, MNRAS, 469, 2434
Boss A. P., 2006, ApJ, 643, 501
Bozza V., 2010, MNRAS, 408, 2188
Bozza V., Bachelet E., Bartolić F., Heintz T. M., Hoag A. R., Hundertmark M., 2018, MNRAS, 479, 5157
Bramich D. M., 2008, MNRAS, 386, L77
Calchi Novati S. et al., 2015a, ApJ, 804, 20
Calchi Novati S. et al., 2015b, ApJ, 814, 92
Calchi Novati S. et al., 2018, AJ, 155, 261
Calchi Novati S. et al., 2019, AJ, 157, 121
Chabrier G., 2003, PASP, 115, 763
Claret A., Bloemen S., 2011, A&A, 529, A75
DePoy D. L. et al., 2003, in Iye M., Moorwood A. F. M., eds, Proc. SPIE Conf. Ser. Vol. 4841, Instrument Design and Performance for Optical/Infrared Ground-based Telescopes. SPIE, Bellingham, p. 827
Dong S. et al., 2007, ApJ, 664, 862
Dong S. et al., 2009, ApJ, 695, 970
Foreman-Mackey D., Hogg D. W., Lang D., Goodman J., 2013, PASP, 125, 306
Fukui A. et al., 2019, AJ, 158, 206
Gaia Collaboration et al., 2016, A&A, 595, A1

Gaia Collaboration et al., 2018, A&A, 616, A1
Gaudi B. S., 1998, ApJ, 506, 533
Gaudi B. S. et al., 2008, Science, 319, 927
Gould A., 1992, ApJ, 392, 442
Gould A., 1994, ApJ, 421, L75
Gould A., 1995, ApJ, 441, L21
Gould A., 2000, ApJ, 542, 785
Gould A., 2004, ApJ, 606, 319
Gould A., 2019, J. Kor. Astron. Soc., 52, 121
Gould A., Loeb A., 1992, ApJ, 396, 104
Gould A. et al., 2020, J. Kor. Astron. Soc., 53, 9
Han C. et al., 2013, ApJ, 778, 38
Han C. et al., 2017, ApJ, 834, 82
Han C. et al., 2020, A&A, 641, A105
Hirao Y. et al., 2020, AJ, 160, 74
Houdashelt M. L., Bell R. A., Sweigart A. V., 2000, AJ, 119, 1448
Hwang K.-H. et al., 2013, ApJ, 778, 55
Hwang K. H. et al., 2018a, J. Kor. Astron. Soc., 51, 197
Hwang K.-H. et al., 2018b, AJ, 155, 20
Ida S., Lin D. N. C., 2005, ApJ, 626, 1045
Jiang G. et al., 2004, ApJ, 617, 1307
Jung Y. K. et al., 2015, ApJ, 798, 123
Jung Y. K. et al., 2018, ApJ, 863, 22
Jung Y. K. et al., 2019, AJ, 158, 28
Kennedy G. M., Kenyon S. J., 2008, ApJ, 673, 502
Kim S.-L. et al., 2016, J. Kor. Astron. Soc., 49, 37
Kim D.-J. et al., 2018, AJ, 155, 76
Koshimoto N., Bennett D. P., 2020, AJ, 160, 177
Kozłowski S., Woźniak P. R., Mao S., Wood A., 2007, ApJ, 671, 420
Kubas D. et al., 2012, A&A, 540, A78
Luhman K. L., 2012, ARA&A, 50, 65
Mao S., 2012, Res. Astron. Astrophys., 12, 947
Mao S., Paczynski B., 1991, ApJ, 374, L37
Nataf D. M. et al., 2013, ApJ, 769, 88
Nemiroff R. J., Wickramasinghe W. A. D. T., 1994, ApJ, 424, L21
Nucita A. A., Licchelli D., De Paolis F., Ingrosso G., Strafella F., Katysheva N., Shugarov S., 2018, MNRAS, 476, 2962
Paczyński B., 1986, ApJ, 304, 1
Poindexter S., Afonso C., Bennett D. P., Glicenstein J.-F., Gould A., Szymański M. K., Udalski A., 2005, ApJ, 633, 914
Poleski R. et al., 2016, ApJ, 823, 63
Poleski R., Penny M., Gaudi B. S., Udalski A., Ranc C., Barentsen G., Gould A., 2019, A&A, 627, A54
Refsdal S., 1966, MNRAS, 134, 315
Reid M. J. et al., 2014, ApJ, 783, 130
Ryu Y.-H. et al., 2018, AJ, 155, 40
Schechter P. L., Mateo M., Saha A., 1993, PASP, 105, 1342
Shin I.-G. et al., 2018, ApJ, 863, 23
Shvartzvald Y. et al., 2017, ApJ, 840, L3
Skowron J. et al., 2018, Acta Astron., 68, 43
Street R. A. et al., 2013, ApJ, 763, 67
Street R. A. et al., 2016, ApJ, 819, 93
Sumi T. et al., 2016, ApJ, 825, 112
Terry S. K. et al., 2021, AJ, 161, 54
Tomaney A. B., Crotts A. P. S., 1996, AJ, 112, 2872
Udalski A., 2003, Acta. Astron., 53, 291
Udalski A., Szymanski M., Kaluzny J., Kubiak M., Mateo M., Krzeminski W., Paczynski B., 1994, AcA, 44, 227
Udalski A., Szymański M. K., Szymański G., 2015a, Acta Astron., 65, 1
Udalski A. et al., 2015b, ApJ, 799, 237
Vandorou A. et al., 2020, AJ, 160, 121
Wang T. et al., 2018, ApJ, 860, 25
Witt H. J., Mao S., 1994, ApJ, 430, 505
Wozniak P. R., 2000, Acta Astron., 50, 421
Wyrzykowski Ł. et al., 2020, A&A, 633, A98
Yee J. C. et al., 2015a, ApJ, 802, 76
Yee J. C. et al., 2015b, ApJ, 810, 155
Yoo J. et al., 2004, ApJ, 603, 139

Zang W. et al., 2018, PASP, 130, 104401
Zang W. et al., 2020a, ApJ, 891, 3
Zang W. et al., 2020b, ApJ, 897, 180
Zhu W. et al., 2015, ApJ, 805, 8
Zhu W. et al., 2017a, PASP, 129, 104501
Zhu W. et al., 2017b, AJ, 154, 210
Zhu W. et al., 2017c, ApJ, 849, L31

SUPPORTING INFORMATION

Supplementary data are available at *MNRAS* online.

Figure 1. The observed data with the best-fitting 2L1S model.
Please note: Oxford University Press is not responsible for the content or functionality of any supporting materials supplied by the authors. Any queries (other than missing material) should be directed to the corresponding author for the article.

[1]*Department of Astronomy and Tsinghua Centre for Astrophysics, Tsinghua University, Beijing 100084, China*
[2]*Department of Particle Physics and Astrophysics, Weizmann Institute of Science, Rehovot 76100, Israel*
[3]*Astronomical Observatory, University of Warsaw, Al. Ujazdowskie 4, PL-00-478 Warszawa, Poland*
[4]*Center for Astrophysics | Harvard & Smithsonian, 60 Garden St,Cambridge, MA 02138, USA*
[5]*Korea Astronomy and Space Science Institute, Daejon 34055, Republic of Korea*
[6]*University of Science and Technology, Korea, (UST), 217 Gajeong-ro Yuseong-gu, Daejeon 34113, Republic of Korea*
[7]*Department of Earth and Space Science, Graduate School of Science, Osaka University, Toyonaka, Osaka 560-0043, Japan*
[8]*National Astronomical Observatories, Chinese Academy of Sciences, Beijing 100101, China*
[9]*IPAC, Mail Code 100-22, Caltech, 1200 E. California Blvd., Pasadena, CA 91125, USA*
[10]*Max-Planck-Institute for Astronomy, Königstuhl 17, D-69117 Heidelberg, Germany*
[11]*Department of Astronomy, Ohio State University, 140 W. 18th Ave., Columbus, OH 43210, USA*
[12]*Canadian Institute for Theoretical Astrophysics, University of Toronto, 60 St George Street, Toronto, ON M5S 3H8, Canada*
[13]*Jet Propulsion Laboratory, California Institute of Technology, 4800 Oak Grove Drive, Pasadena, CA 91109, USA*
[14]*Division of Physics, Mathematics, and Astronomy, California Institute of Technology, Pasadena, CA 91125, USA*
[15]*Department of Physics, University of Warwick, Gibbet Hill Road, Coventry CV4 7AL, UK*
[16]*University of Canterbury, Department of Physics and Astronomy, Private Bag 4800, Christchurch 8020, New Zealand*
[17]*Department of Physics, Chungbuk National University, Cheongju 28644, Republic of Korea*
[18]*School of Space Research, Kyung Hee University, Yongin, Kyeonggi 17104, Republic of Korea*
[19]*Institute of Natural and Mathematical Sciences, Massey University, Auckland 0745, New Zealand*
[20]*Institute for Space-Earth Environmental Research, Nagoya University, Nagoya 464-8601, Japan*
[21]*Code 667, NASA Goddard Space Flight Center, Greenbelt, MD 20771, USA*
[22]*Department of Astronomy, University of Maryland, College Park, MD 20742, USA*
[23]*Department of Physics, University of Auckland, Private Bag 92019, Auckland, New Zealand*
[24]*Department of Earth and Planetary Science, Graduate School of Science, The University of Tokyo, 7-3-1 Hongo, Bunkyo-ku, Tokyo 113-0033, Japan*

[25]*Instituto de Astrofísica de Canarias, Vía Láctea s/n, E-38205 La Laguna, Tenerife, Spain*

[26]*Department of Astronomy, Graduate School of Science, The University of Tokyo, 7-3-1 Hongo, Bunkyo-ku, Tokyo 113-0033, Japan*

[27]*National Astronomical Observatory of Japan, 2-21-1 Osawa, Mitaka, Tokyo 181-8588, Japan*

[28]*School of Chemical and Physical Sciences, Victoria University, Footscray VIC 3011, Wellington, New Zealand*

[29]*Institute of Space and Astronautical Science, Japan Aerospace Exploration Agency, 3-1-1 Yoshinodai, Chuo, Sagamihara, Kanagawa, 252-5210, Japan*

[30]*University of Canterbury Mt. John Observatory, PO Box 56, Lake Tekapo 8770, New Zealand*

[31]*Department of Physics, Faculty of Science, Kyoto Sangyo University, 603-8555 Kyoto, Japan*

[32]*Las Cumbres Observatory Global Telescope Network, 6740 Cortona Drive, suite 102, Goleta, CA 93117, USA*

[33]*Zentrum für Astronomie der Universität Heidelberg, Astronomisches Rechen-Institut, Mönchhofstr. 12-14, D-69120 Heidelberg, Germany*

[34]*Facultad de Ingeniería y Tecnología, Universidad San Sebastian, General Lagos 1163, Valdivia 5110693, Chile*

[35]*School of Physics and Astronomy, Tel-Aviv University, Tel-Aviv 6997801, Israel*

[36]*Department of Physics and Astronomy, Louisiana State University, Baton Rouge, LA 70803, USA*

This paper has been typeset from a TEX/LATEX file prepared by the author.